Supporting Information

Observing Single-Atom Catalytic Sites During Reactions with Electrospray Ionization Mass Spectrometry

Max J. Hülsey, Geng Sun, Philippe Sautet, and Ning Yan*

anie_202011632_sm_miscellaneous_information.pdf

Methods

Synthesis and characterization of $K_7PW_{11}O_{39}$. A bottom-up approach was used for the synthesis of the lacunary POM as reported before.[1] 18.15 g sodium tungstate dihydrate (SCR), 8.8 mL glacial acetic acid (Merck, reagent grade) and 5 mL phosphoric acid (VWR, reagent grade) were dissolved in 30 mL deionized water under reflux conditions. After 2 h under reflux conditions, the mixture was cooled down, 6 g potassium chloride (ACS reagent, Sigma Aldrich) were added, and the mixture was kept stirring for 1 h at room temperature. The precipitated solid was separated by filtration and further washed three times with small amounts of hot water. Mixing the solid with 5 mL deionized water and 1 g potassium chloride under reflux conditions and subsequent slow crystallization improved the product purity. This reprecipitation was repeated for three times and the final obtained solid was dried in an oven overnight. The purity of the sample was confirmed by Attenuated total reflectance infrared spectroscopy (ATR-IR) using a Nicolet iS50 FT-IR spectrometer with a resolution of 4 cm^{-1} between 525-4000 cm^{-1} averaged over 32 scans. Phosphotungstic acid hydrate (Sigma Aldrich, reagent grade) and sodium tungstate dihydrate were used as reference materials. ESI-MS was used to confirm purity as further described below. NMR analyses were conducted on a Bruker 400 MHz UltraShield Plus spectrometer in a 1:1 $H_2O:D_2O$ mixture (99.9% D labelled, Cambridge Isotope Laboratories).

Catalytic reactions. For the CO oxidation reaction, 33 mg $K_7PW_{11}O_{39}$ in 20 mL deionized water were mixed with 28.8 μL rhodium nitrate solution (10 wt%, in dilute nitric acid). Carbon monoxide (5% in argon, Air Liquide) was then bubbled through the solution with a flow rate of 100 cm^3 min^{-1} for up to 1 h at room temperature. The gas flow was switched to oxygen (5% in argon, Air Liquide) with a flow rate of 100 cm^3 min^{-1} and the reaction was continued for up to 24 h at room temperature or at 70 °C (using a water bath) for 4 h. Samples were taken at set time points, were transported in a gas tight container and immediately analyzed by ESI-MS (vide infra).

All catalytic alcohol oxidation reactions were performed in thick walled open glass vessel using in situ formed catalysts. For the catalyst formation, 33 mg $K_7PW_{11}O_{39}$ were dissolved in 20 mL deionized water. Appropriate amounts of metal nitrate salt or solution were added to achieve a 1:1 $PW_{11}O_{39}$:metal ratio including: chromium nitrate nonahydrate (≥99.99% trace metal basis), manganese nitrate hydrate (99.99% trace metal basis), iron nitrate nonahydrate (≥99.95% trace metal basis), cobalt nitrate hexahydrate (99.999% trace metal basis), nickel nitrate hexahydrate (99.999% trace metal basis), copper nitrate hemi(pentahydrate) (≥99.99% trace metal basis), zinc nitrate hexahydrate (purum, ≥99.0), rhodium nitrate solution (10 wt%, in dilute nitric acid), palladium nitrate dihydrate, silver nitrate (99.9999% trace metal basis), cerium nitrate hexahydrate (99.99% trace metal basis), indium nitrate hydrate (99.99% trace metal basis), bismuth nitrate pentahydrate (≥ 99.99% trace metal basis) (all obtained from Sigma Aldrich), and platinum nitrate solution (Alfa Aesar, 15 wt%). The reaction mixture was heated to 70 °C and kept stirring at 800 rpm for 20 min upon which 50 μL benzyl alcohol (Sigma Aldrich, ACS reagent ≥ 99.0%) and 100 μL hydrogen peroxide (Sigma Aldrich, 30 wt%) were added. The reaction mixture was stirred (800 rpm) at 70 °C for 5 hours and samples were taken from the solution, mixed with a spatula tip of sodium sulfite and analyzed by gas chromatography (GC) using an Agilent 7890A equipped with an SGE GC Column BP5 (15 m x 0.53 mm inner diameter, 1.50 μm film) column and a flame ionization detector. Benzoic acid was not observed as a side product and thus the selectivity for benzaldehyde can be assumed to exceed 98%. For ESI-MS analysis, samples were directly taken out of the solution,

transported in a gas tight container and immediately analyzed by ESI-MS (vide infra). Benzyl alcohol derivatives have been used including 4-nitrobenzyl alcohol (Sigma Aldrich, 99%) and 4-methoxybenzyl alcohol (Sigma Aldrich, 98%).

ESI-MS measurements. All ESI-MS analyses were performed using a Hamilton gas tight syringe in a kd Scientific syringe pump connected to a Bruker MicroTOF-Q system with a liquid flow rate of 180 µL h^{-1}. The ESI-MS source was operated with an end plate offset of 500 V, a capillary potential of 3.8 kV, a nebulizer gas (N$_2$) pressure of 0.4 bar with a drying gas (N$_2$) flow of 4 L min^{-1} at a temperature of 200 °C. All analyses were done in the negative mode with the accumulation of data for 1 min with a 1 Hz spectrum collection rate between m/z 50 and 3000. MS/MS was done using the multiple reaction monitoring (MRM) method where a specific precursor ion from the first mass separator is fragmented by Ar gas with increasing collision energies. External calibration of the ESI-MS was done using a sodium formate solution while internal calibration against the ubiquitous peak for $\{PW_{11}O_{39}{}^{7-} + 3H^+ + Na^+\}^{3-}$ with the highest intensity peak at m/z 900.75 was used. Residual errors are in the range of m/z 0.05 with a common full width at half maximum value of around m/z 0.1. Typically, reaction solutions measured by ESI-MS did not contain inorganic compounds in concentrations above 1 mM. After each measurement, the syringe, tubing and ESI needle were cleaned with ultrapure water and 50% 2-propanol (HPLC grade 99.9%, Sigma Aldrich) until the most dominant peaks exhibited intensities ≤ 100 (peak intensities during measurements were normally in the range of 10^4-10^5). Kinetic measurements were done similar to the reaction described above with increasing temperatures inside a two-necked reaction flask. The temperature inside the solution was measured directly before ESI-MS analysis using a thermometer and samples were immediately injected into the ESI-MS with delays <30 s. For the activation energy determination, the change in relative concentrations of each of the intermediates were estimated by averaging the three most intense m/z peaks which are seen to deviate less than 5%. Although absolute concentrations are not straight forward to determine, relative concentrations of different intermediates can be quantified especially when they appear in a similar m/z range (within m/z 50-100) as has been demonstrated previously.[2] Abbreviations for the various ESI-MS detected species were used as follows: {[(Active single-atom site of the catalyst including the oxidation state)(adsorbate on the single-atom site)(POM)(POM-based adsorbates)]cations masking some of the negative charges}$^{\text{total charge of the molecular ion}}$.

DFT calculations. In the theoretical simulations, we have adopted two models: negatively charged $PW_{11}O_{39}Rh_1$ and neutral $H_4PW_{11}O_{39}Rh_1$. For the charged model, the energies and forces are computed by CP2K package with triple-ζ *molecularly optimized basis functions* (TZVP-MOLOPT),[3] which have been shown to present only very small basis set superposition error.[3b] The energy cutoff for auxiliary plane waves is 400 Ry, and the SCF convergence criterion is 1.0E-7 Ry. All the neutral models are simulated by Vienna Ab initio Simulation Package (VASP),[4] in which the basis sets are expanded with plane waves up to 400 eV. The structure optimizations are conducted by ASE package[5] with BFGS method until the maximum force residue is below 0.03 eV/Angstrom. All the structure optimizations are conducted with spin-polarized calculations. We have tested both singlet and triplet state as initial guess for Rh(III) and R(I) species, but the SCFs only converge to the singlet state. The transition states are optimized by NEB[6] method and DIMER[7] method.

In all simulations, the exchange-correlation interaction of electrons is approximated in the level of generalized gradient approximation with Perdew–Burke-Ernzerhof functional.[8] Density functional theory with GGA functional has been extensively used in studying the structures

and reactivities of polyoxometalates, exemplary papers are from J. M. Poblet group[9] and more details are also discussed in the review.[10] In J.M. Poblet's papers, they mostly use the BP86 functional which is very similar to the PBE functional in a broad range of chemical properties.[11] The PBE functional is has also been used in recent years and the results show that PBE is accurate in predicting the structures and nature of frontier molecular orbitals of the α-Keggin type polyoxometalate.[12] However, we should note that if the accurate orbital energies are required (such as energy of lowest unoccupied molecular orbital), then hybrid functionals (see the paper by Wu et al.) with a fraction of exact exchange will be beneficial.[12]
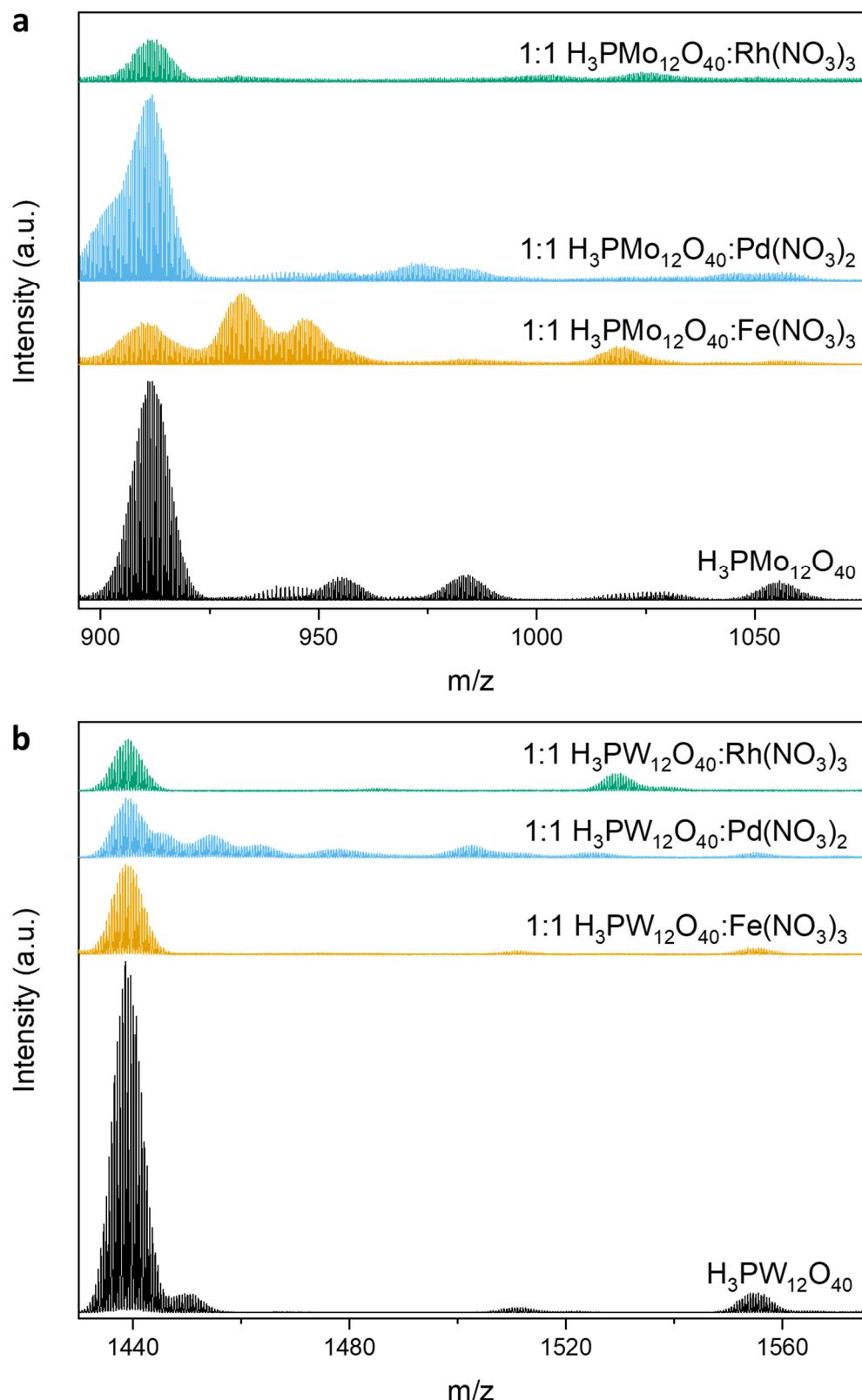
Figure S1. ESI-MS of different 1:1 molar combinations of $H_3PMo_{12}O_{40}$ and $H_3PW_{12}O_{40}$ with $Fe(NO_3)_3$, $Pd(NO_3)_2$, and $Rh(NO_3)_3$.
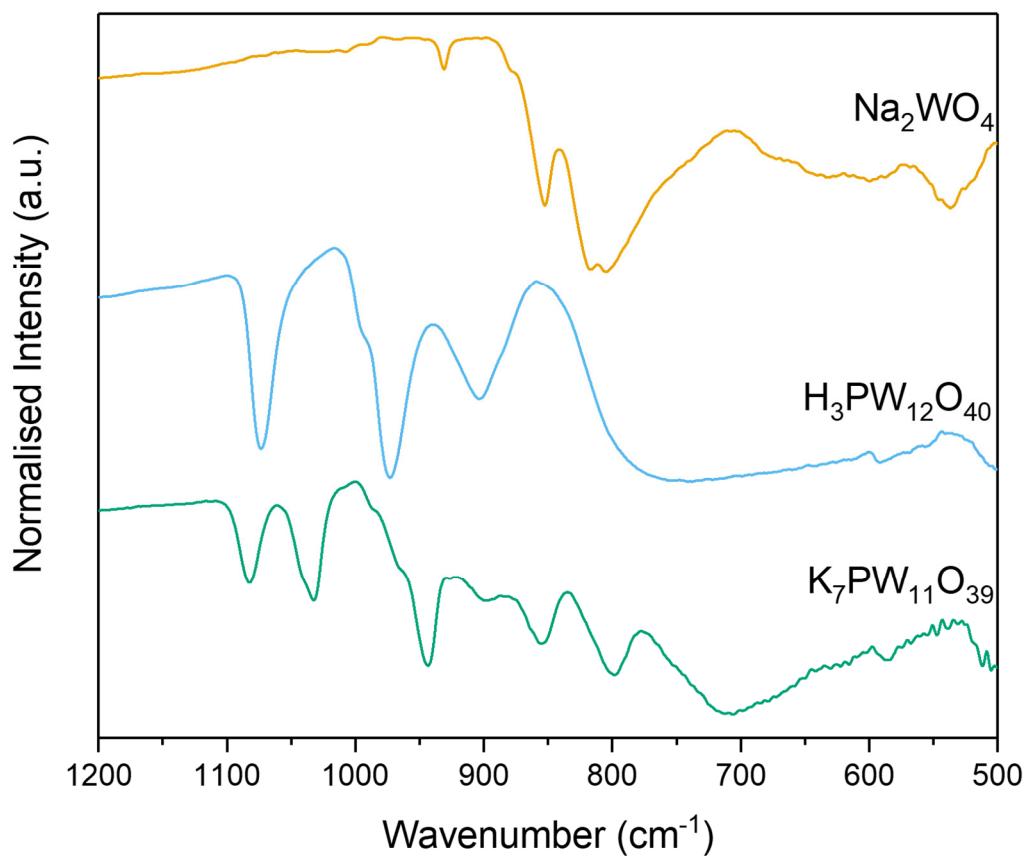
Figure S2. Infrared spectroscopy of $K_7PW_{11}O_{39}$ and reference samples. Characteristic vibrations at 1082 (s), 1033 (s), 944 (s), 855 (s), 798 (s) and 706 (b) cm^{-1} were observed for $K_7PW_{11}O_{39}$.[13]
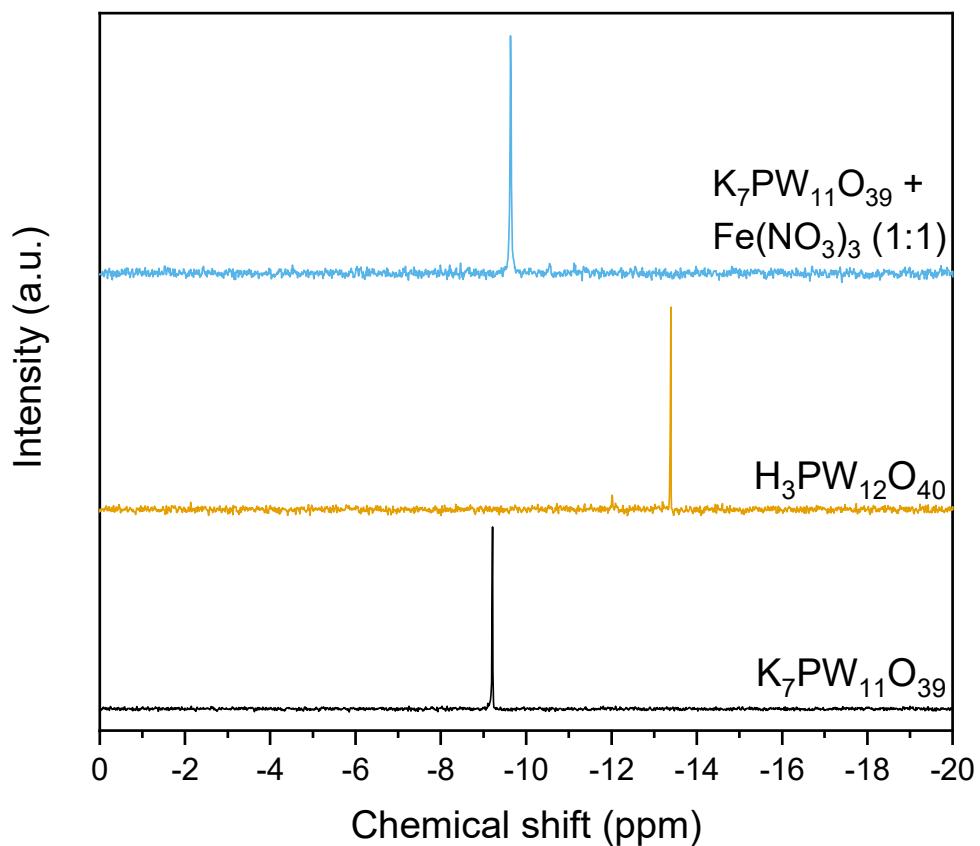
Figure S3. ^{31}P NMR of POM-based precursors and catalysts. All chemical shifts are reported relative to H_3PO_4 as external reference.
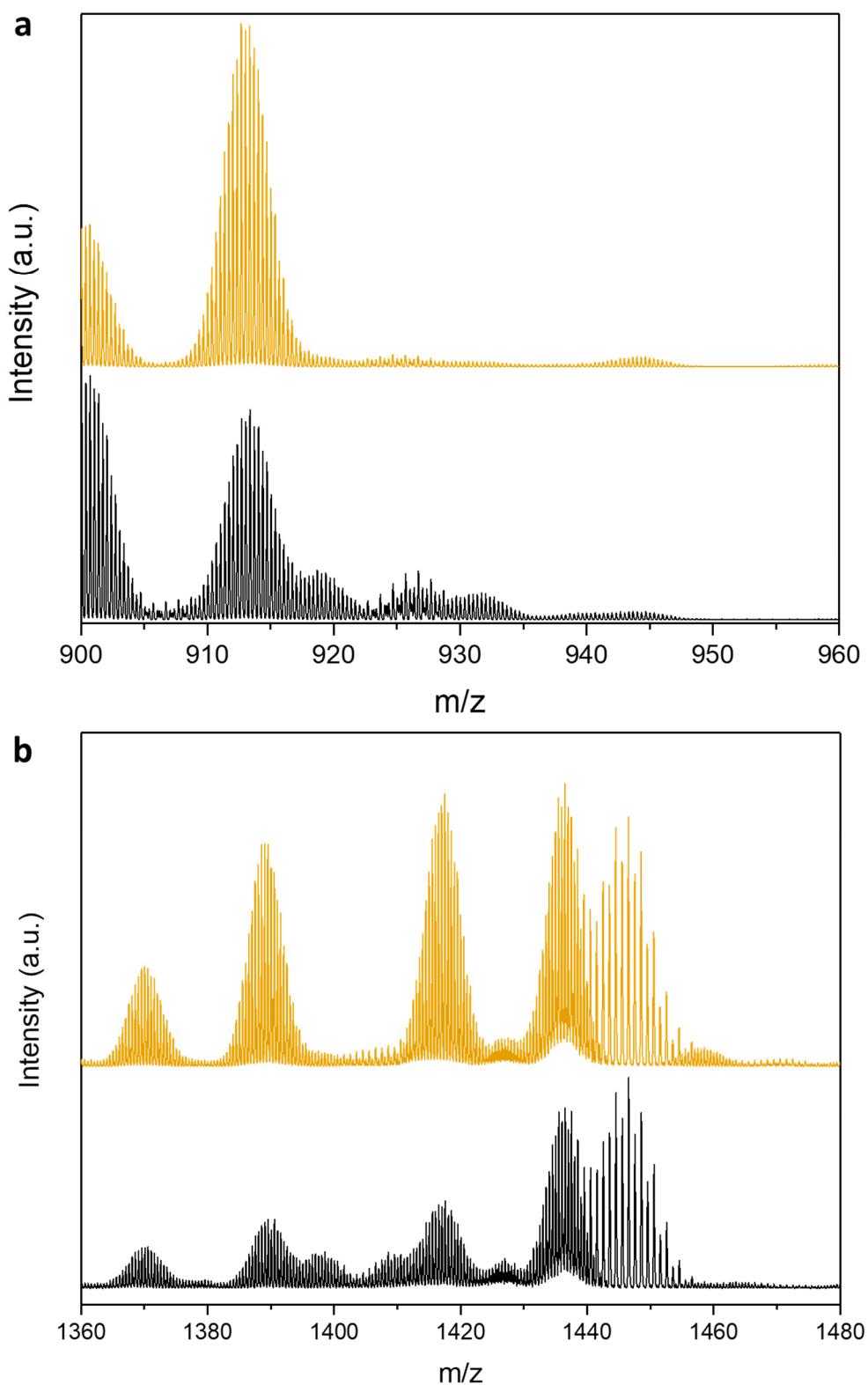
Figure S4. ESI-MS spectra for $PW_{11}O_{39}$ before (black) and after 1 h CO treatment (orange). (a) z = 3 and (b) z = 2 range. Reactions were carried out in a V_{total} = 0.02 L DI water with $C_{PW_{11}O_{39}}$ = 0.5 mM and F_{total} = 100 cm^3 min^{-1} of CO (5:95 CO:Ar) at a p_{total} = 1 bar and room temperature. Although small differences in the mass spectra can be observed, no additional peaks assignable to CO-adsorbed POM species appeared.
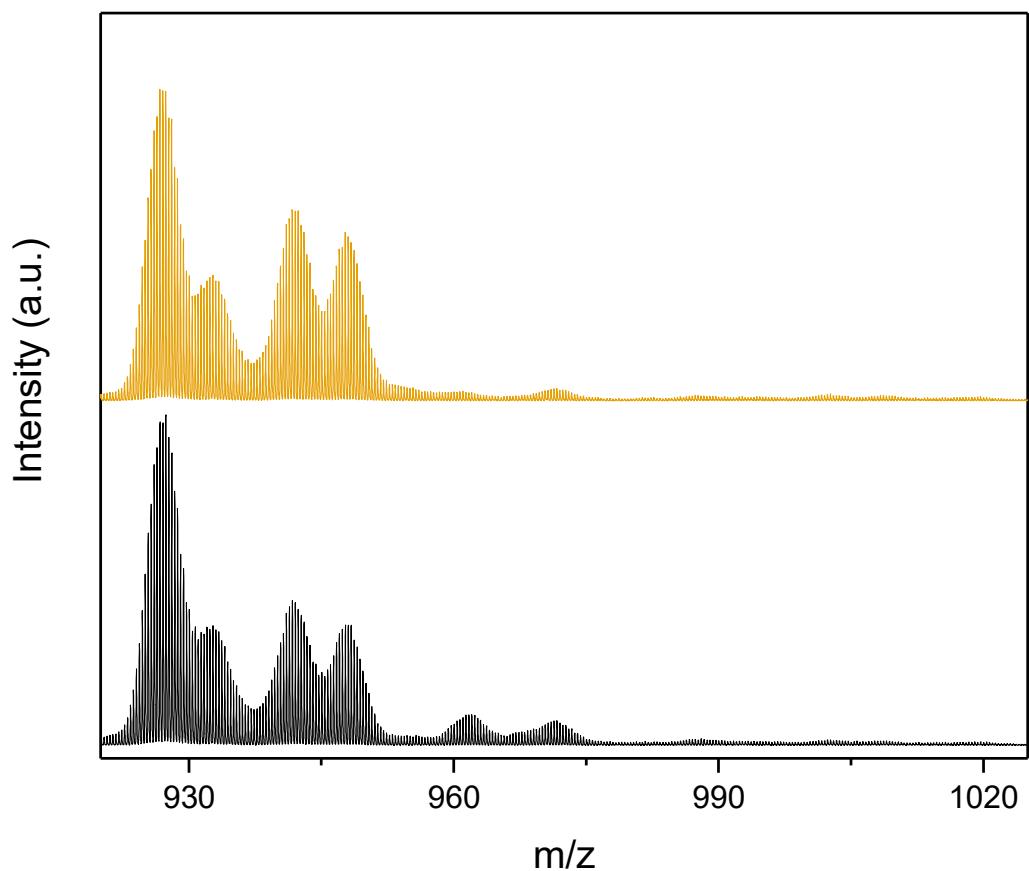
Figure S5. ESI-MS spectrum of $PW_{11}O_{39}Rh_1$ before (black) and after (orange) O_2 exposure. Reactions were carried out in a V_{total} = 0.02 L DI water with $C_{PW_{11}O_{39}}$ = 0.5 mM and C_{Rh} = 0.5 mM and F_{total} = 100 cm^3 min^{-1} of 5:95 O_2:Ar at a p_{total} = 1 bar and room temperature for 30 min.
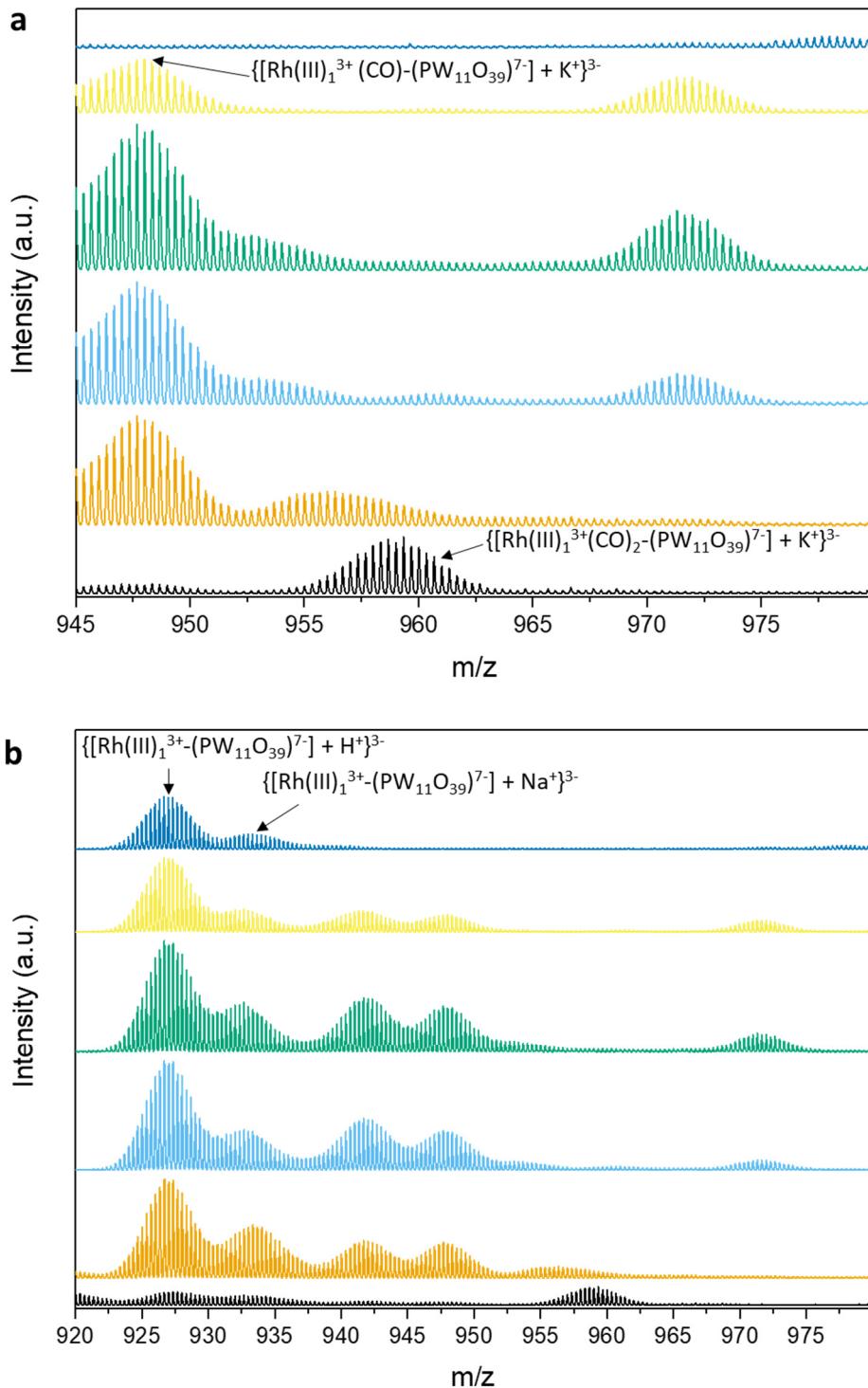
Figure S6. ESI-MS spectra for $PW_{11}O_{39}Rh_1$ after treatment under different reaction conditions. Same order for both (a) and (b) from bottom to top: 2 min CO (black), 1 h CO (orange), 1 h CO and 2 min O_2 (light blue), 1 h CO and 1 h O_2 (green), 1 h CO and 24 h O_2 (yellow), and 1 h CO and 4 h O_2 at 70 °C (dark blue) at different ranges: a 945 to 980 m/z, and b 920 to 980 m/z. Especially after treatment with 1 h CO and 4 h O_2 at 70 °C, an almost pure $PW_{11}O_{39}Rh_1$ sample was recovered. Reactions were carried out in a V_{total} = 0.02 L DI water with $C_{PW_{11}O_{39}}$ = 0.5 mM and C_{Rh} = 0.5 mM and F_{total} = 100 cm^3 min^{-1} of each gas (5:95 CO:Ar and 5:95 O_2:Ar) at a p_{total} = 1 bar and room temperature.
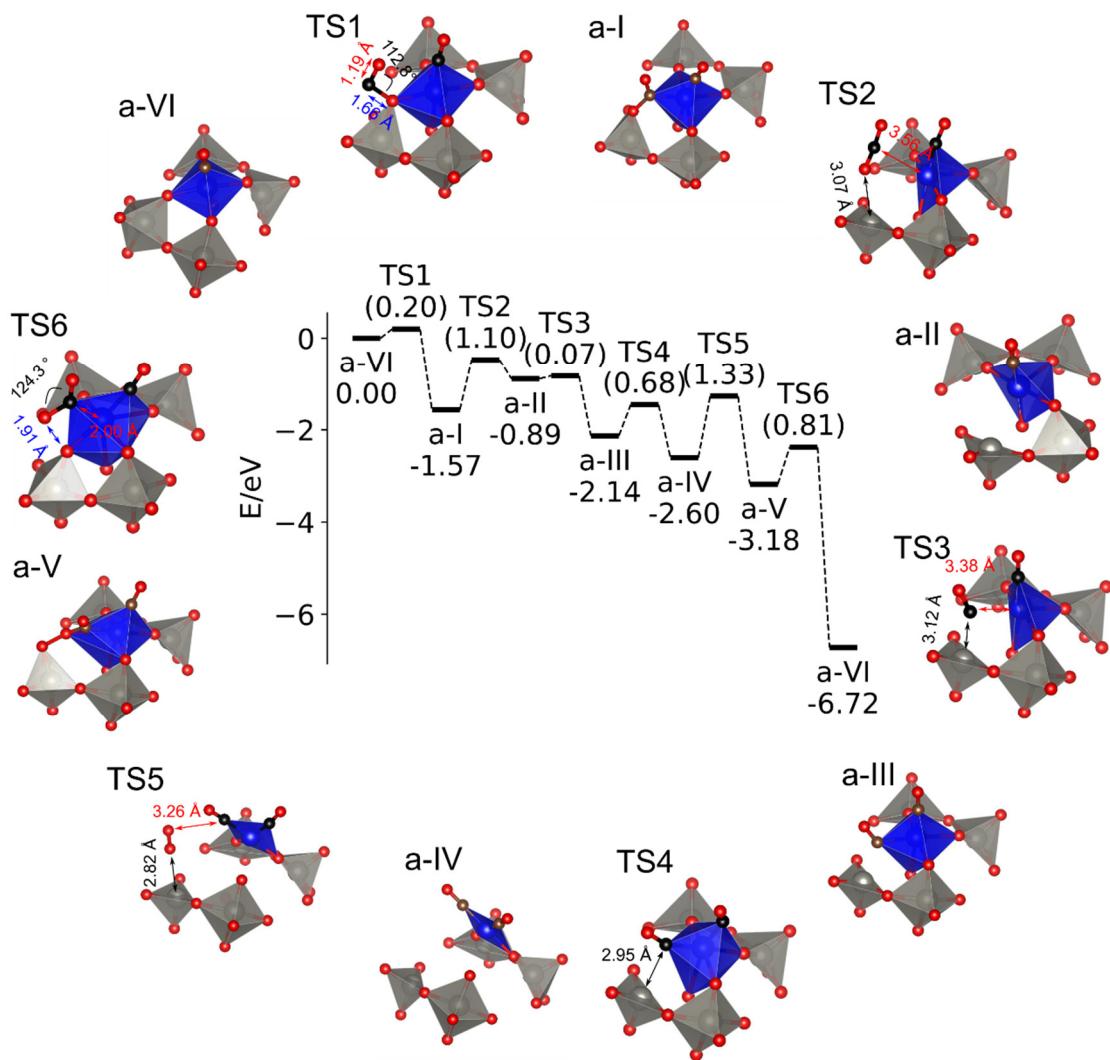
**Figure S7.** Calculated CO oxidation mechanism on $PW_{11}O_{39}Rh_1$ (charge 4-) with the energy profile in the center. **a-I** to **a-VI** are reaction intermediates and TS1-TS6 are transition states. For clarity, only a part of the POM support is shown for each structure. The color code is: Rh (blue), W(grey), O(red), C(black). The numbers in parenthesis is the activation barrier for each elementary step, and the numbers below the label **a-X** are energies of each intermediate using **a-VI** plus gas phase reactant as reference.

Table S1. Comparison of the net charge located on Rh for various catalyst states and rhodium complexes.

Species	DDEC6[14]
a-I	0.878
a-II	0.480
a-III	0.903
a-IV	0.360
a-V	0.955
a-VI	1.225
$[RhCl_6]^{3-}$	1.000
$[Rh(H_2O)_6]^{3+}$	1.223
$RhCl_3(H_2O)_3$	0.831
$RhCl(H_2O)_3$	-0.082
$RhCl(PH_3)_3$	-0.252

Based on the charge analysis, it becomes obvious that during the formation of the oxygen vacancy (transformation of **a-I** to **a-II**), the charge on Rh (q(Rh)) reduces significantly from 0.878 to 0.480. During the formation of the presumably very short-lived intermediate **a-III**, the q(Rh) increases again to 0.903 while the oxygen vacant structure **a-IV** has a q(Rh) value of 0.360 which is almost 3 times lower than the value for **a-I** (0.878). Upon refill of the oxygen vacancy, the q(Rh) immediately increases again. Although those effects are more pronounced for simple Rh(III) and Rh(I) complexes, the trend is consistent with an intermittent formation of Rh(I) species during the CO oxidation reaction while the initial and final states contain Rh(III).
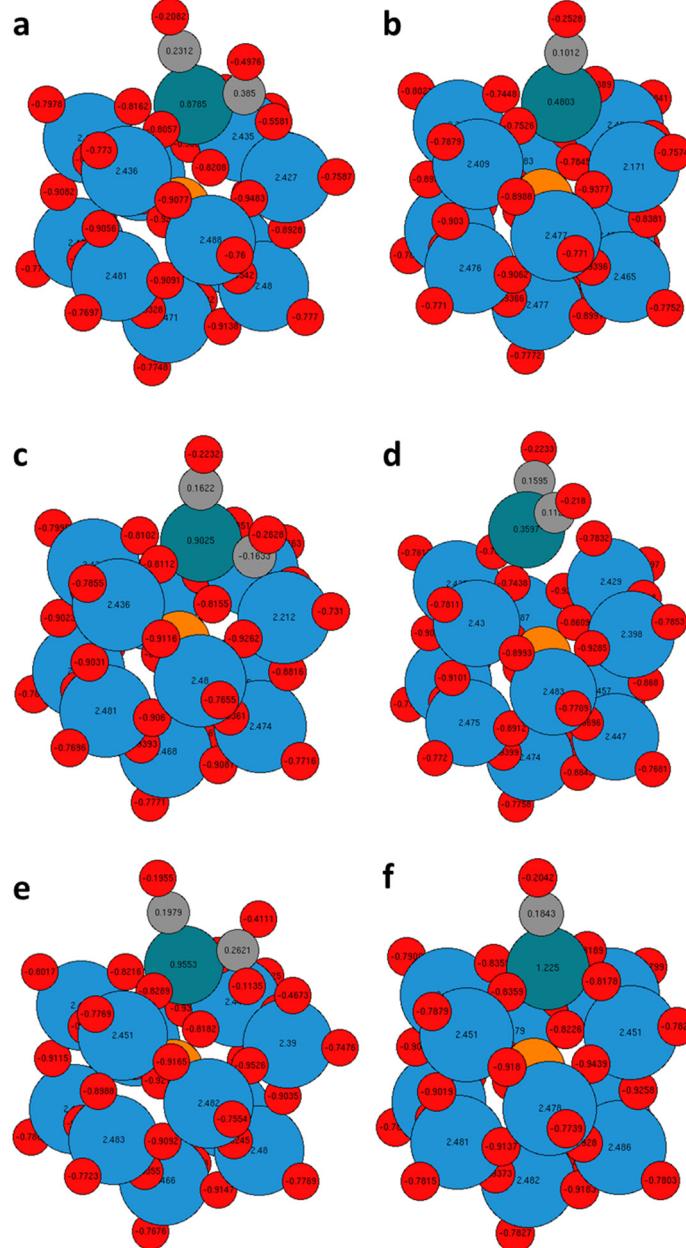
Figure S8. Detailed charge analysis of different catalyst intermediates based on the DDEC6 method. (a) a-I, (b) a-II, (c) a-III, (d) a-IV, (e) a-V, (f) a-VI.

The most dominant changes in the charge density across the POM-based Rh SAC intermediates appear in close proximity to the active site/oxygen vacancy. Besides changes in the charge density of Rh, the tungsten atom adjacent to the oxygen vacancy also experience a reduction of their charge density from 2.427 to 2.171 during the transformation of **a-I** to **a-II**. This change is relatively small (~10% of the total charge density) and thus a change in the formal oxidation state from W(VI) to W(V) or W(IV) should not be expected. Upon refill of the oxygen vacancy, the charge density of the W atom adjacent to the oxygen vacancy returns to the initial value.
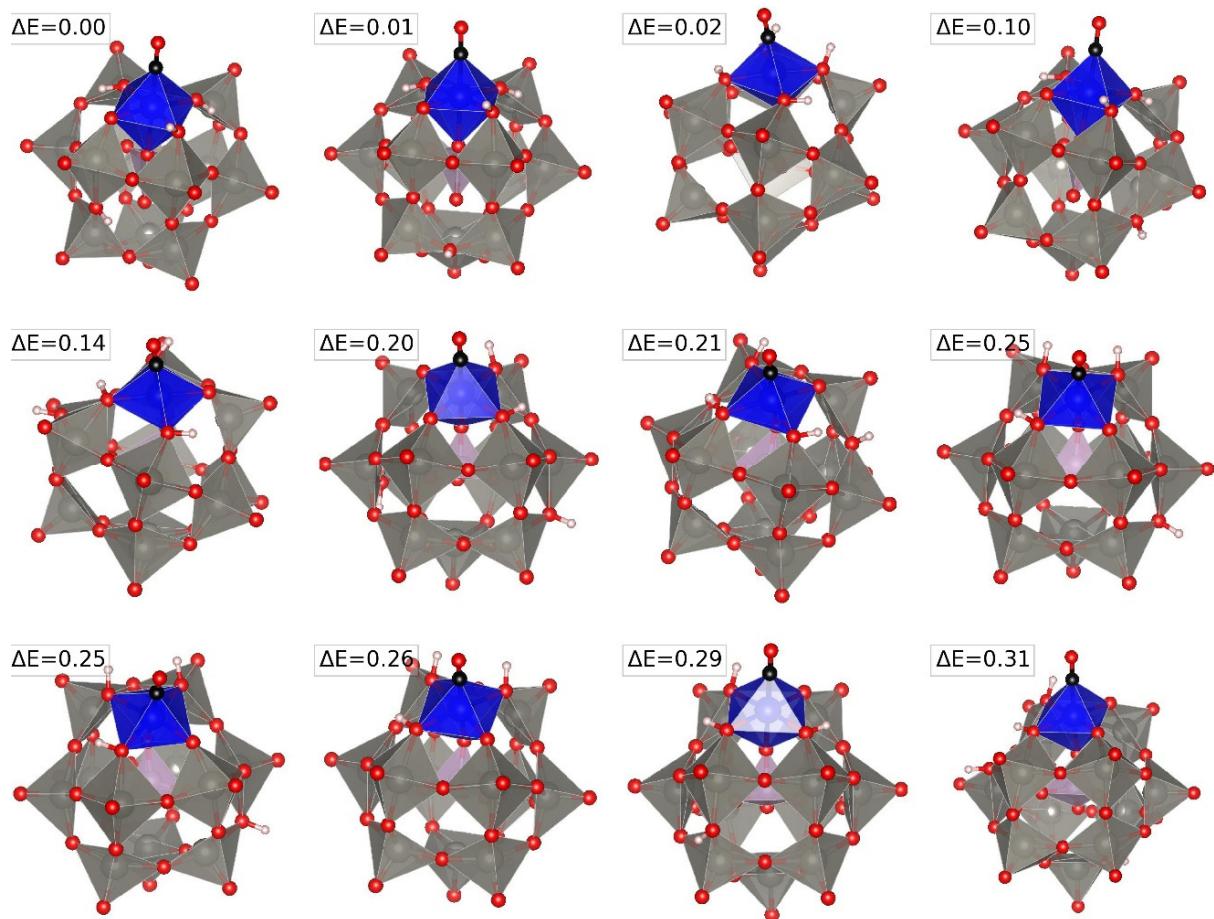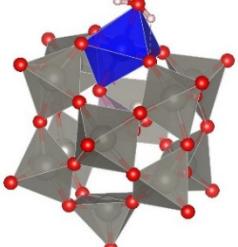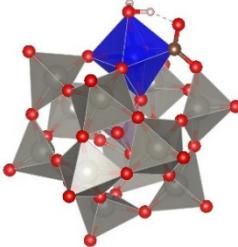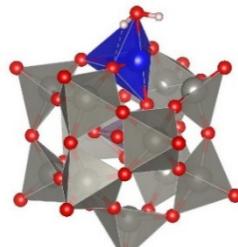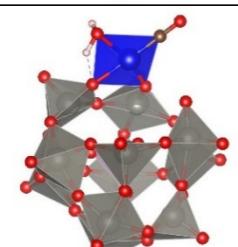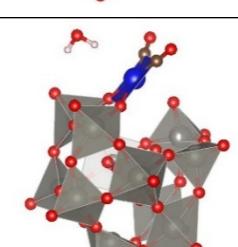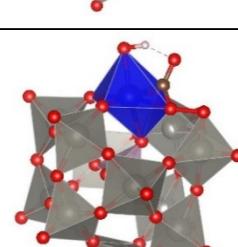
Figure S9. Structures of protonated neutral $PW_{11}O_{39}Rh_1$ models. 138 structures are sampled with different locations for protons. Only the first 12 low energy structures are shown. Color legend: blue polyhedra: Rh, red balls: O, small white balls: H, grey polyhedra: W, pink polyhedra: P, black balls carbons. The energy differences of each structure (using the optimal one as reference, unit eV) are shown on the upper left conner of each figure.

Table S2. Formation energies of water as adsorbate to replace (or co-adsorb) on the reaction intermediates show in the Figure 4 and Figure S8 (a-I to a-VI).

index	Structure	reaction equation	reaction energies/eV
s-VI		a-VI + water -> s-VI + CO	1.455
s-I		a-I + water -> s-I + CO	1.258
s-II		a-II + water -> s-II +CO	2.102
s-IV		a-IV + water -> s-IV + CO	2.004
s-IV-2		a-IV + water-> s-IV-2	-0.549
s-V		a-V + water-> s-V + CO	1.468
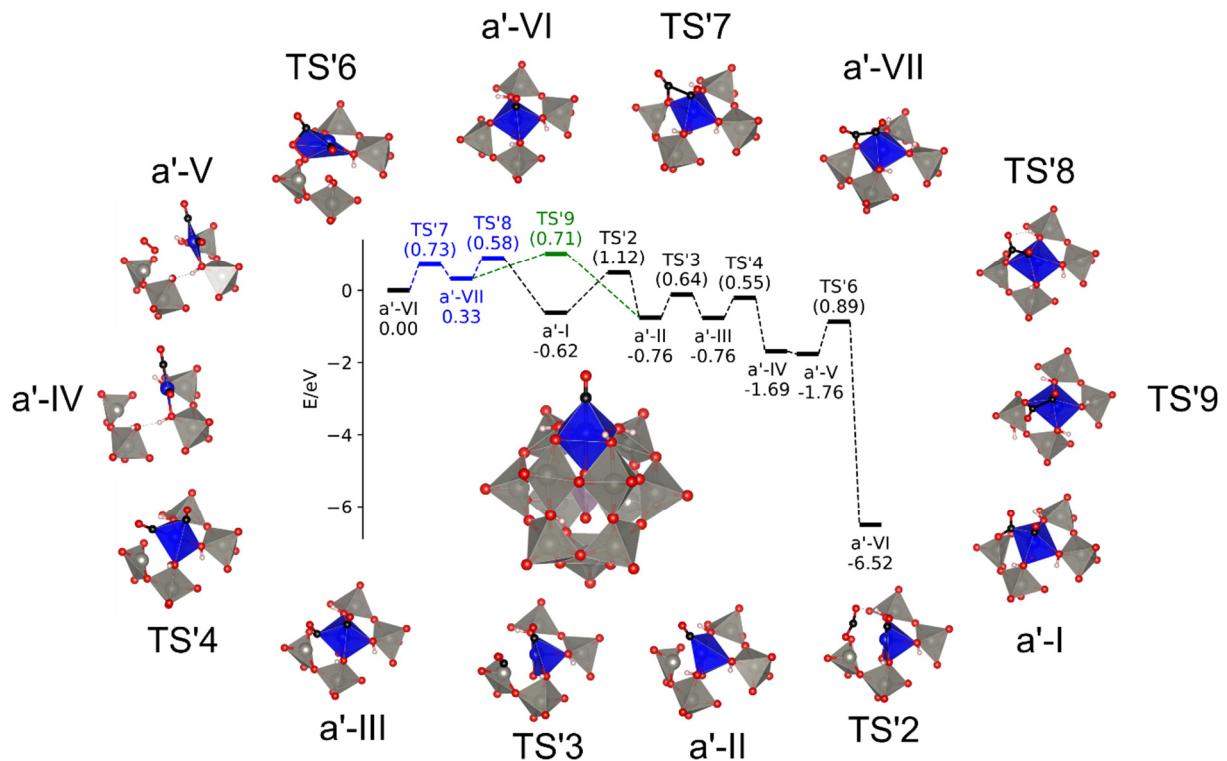
**Figure S10.** Calculated CO oxidation mechanism on protonated neutral $H_4PW_{11}O_{39}Rh_1$ with the energy profile in the center. a'-I to a'-VII are reaction intermediates and TS'1-TS'9 are transitions state structures. The structures are a'-I to a'-VI, TS'-1 to TS'-6 are counterparts of intermediates or transition states in Figure S8, however a'-VII, TS'7, TS'-8, TS'-9 are pathways that only appear with counterions. Red balls are oxygens, black balls are carbons, small white balls are hydrogen atoms. Rh cations are shown with blue polyhedra. W cations are shown in grey polyhedra. The structure in the central part of the figure is the optimal structure with protons.

Table S3. Comparison of different $PW_{11}O_{39}M_1$ catalysts for the benzyl alcohol oxidation reaction.

Metal	TOF (h^{-1})
$PW_{12}O_{40}$	0.14*
$PW_{11}O_{39}Cr_1$	1.45
$PW_{11}O_{39}Mn_1$	1.75
$PW_{11}O_{39}Fe_1$	4.4
$PW_{11}O_{39}Co_1$	1.2
$PW_{11}O_{39}Ni_1$	0.95
$PW_{11}O_{39}Cu_1$	1.7
$PW_{11}O_{39}Zn_1$	0.7
$PW_{11}O_{39}Rh_1$	3.25
$PW_{11}O_{39}Pd_1$	5
$PW_{11}O_{39}Ag_1$	4.85
$PW_{11}O_{39}Pt_1$	2.3
$PW_{11}O_{39}In_1$	2.91
$PW_{11}O_{39}Bi_1$	0.8
$PW_{11}O_{39}Ce_1$	0.64

Reaction conditions: V_{total} = 0.02 L deionized water with $C_{PW11O39}$ = 0.5 mM, C_{Metal} = 0.5 mM, C_{BnzOH} = 25 mM, and C_{H2O2} = 50 mM at T = 70 °C under magnetic stirring at 800 rpm.
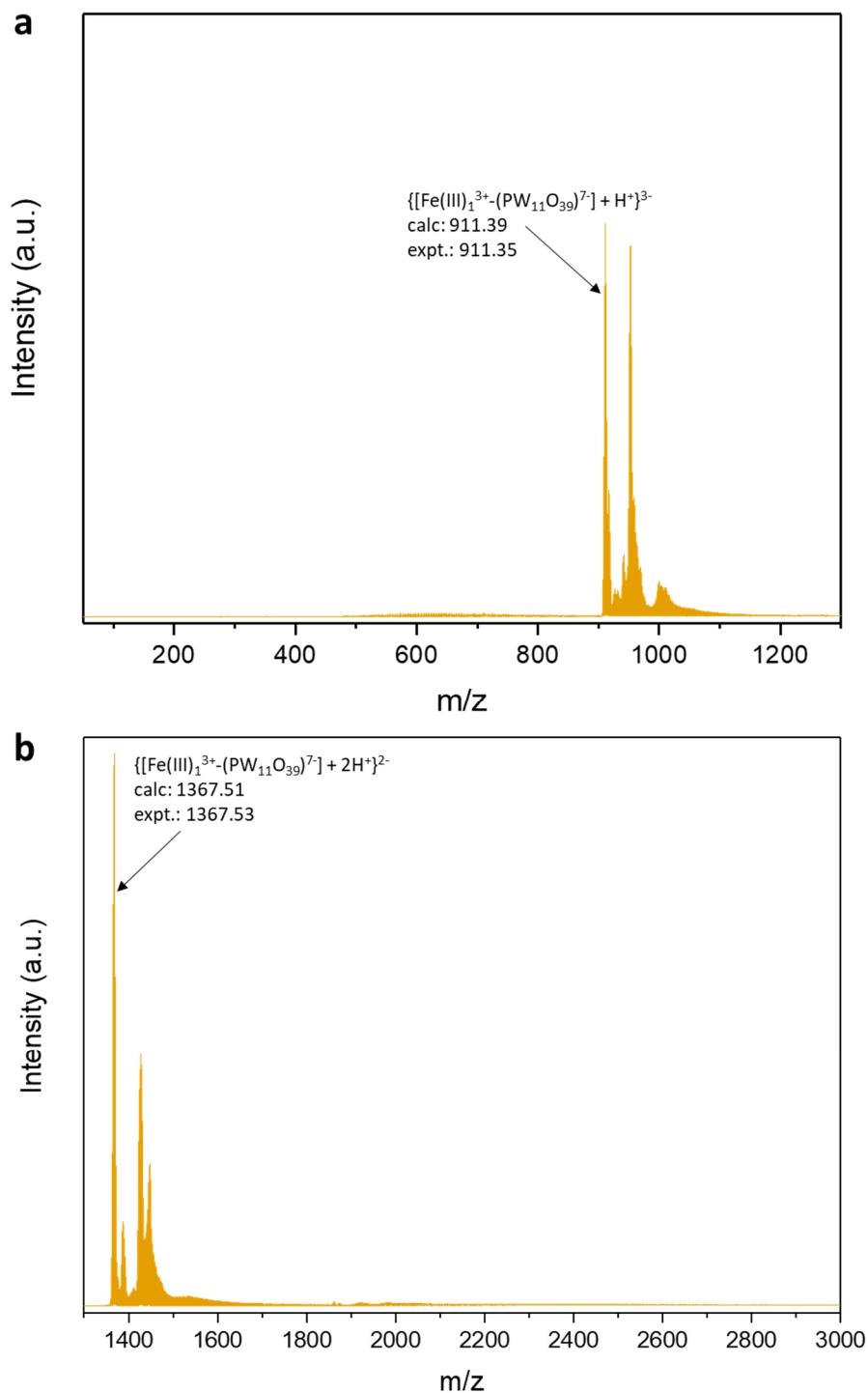
Figure S11. ESI-MS spectrum of $PW_{11}O_{39}Fe_1$ after benzyl alcohol oxidation reaction. The spectrum is shown in the region (a) 50-1300, and (b) 1300-3000. Reaction conditions: V_{total} = 0.02 L deionized water with $C_{PW_{11}O_{39}}$ = 0.5 mM, C_{Fe} = 0.5 mM, C_{BnzOH} = 25 mM, and $C_{H_2O_2}$ = 50 mM at T = 70 °C for 5 h under magnetic stirring at 800 rpm. No decomposition products at low molecular weights can be observed but instead only $PW_{11}O_{39}Fe_1$-derived species at z = 3 (a) and z = 2 (b) were visible.
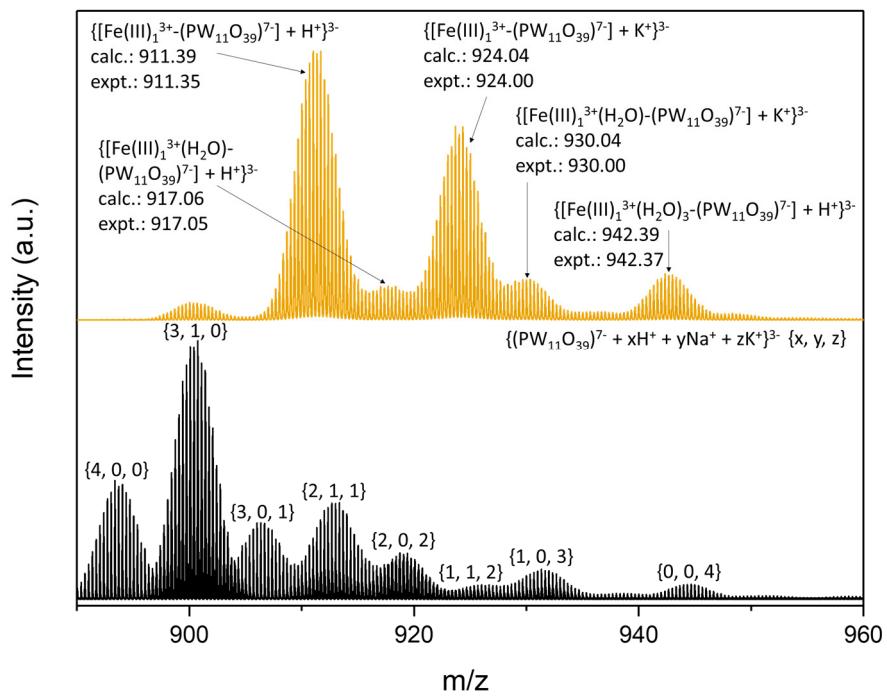
**Figure S12.** ESI-MS spectra for $PW_{11}O_{39}$ and $PW_{11}O_{39}Fe_1$. $PW_{11}O_{39}$ (black) with the respective cation envelope for z = 3. $PW_{11}O_{39}Fe_1$ (orange) with a much-reduced cation envelope due to the adsorption of trivalent Fe(III). For $PW_{11}O_{39}Fe_1$, significant water bonding can be observed. Those water molecules were presumably bound to Fe as for Rh supported on the same POM, no such water binding was observed.
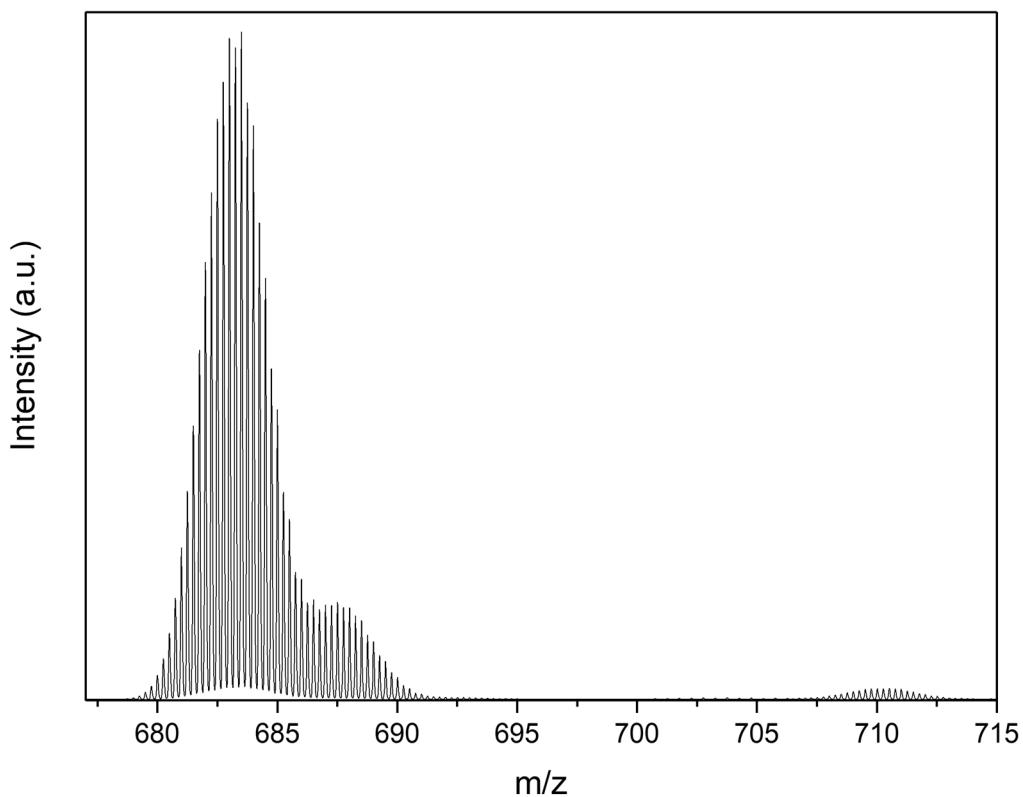
**Figure S13.** ESI-MS spectra of $PW_{11}O_{39}Fe_1$ mixed with benzyl alcohol. Reaction conditions for the adsorption experiments: V_{total} = 0.02 L deionized water with $C_{PW_{11}O_{39}}$ = 0.5 mM, C_{Fe} = 0.5 mM, C_{BnzOH} = 5 mM at room temperature for 10 min under magnetic stirring at 800 rpm. Samples for the adsorption reaction solutions were immediately injected into the ESI-MS with delays < 30 s.
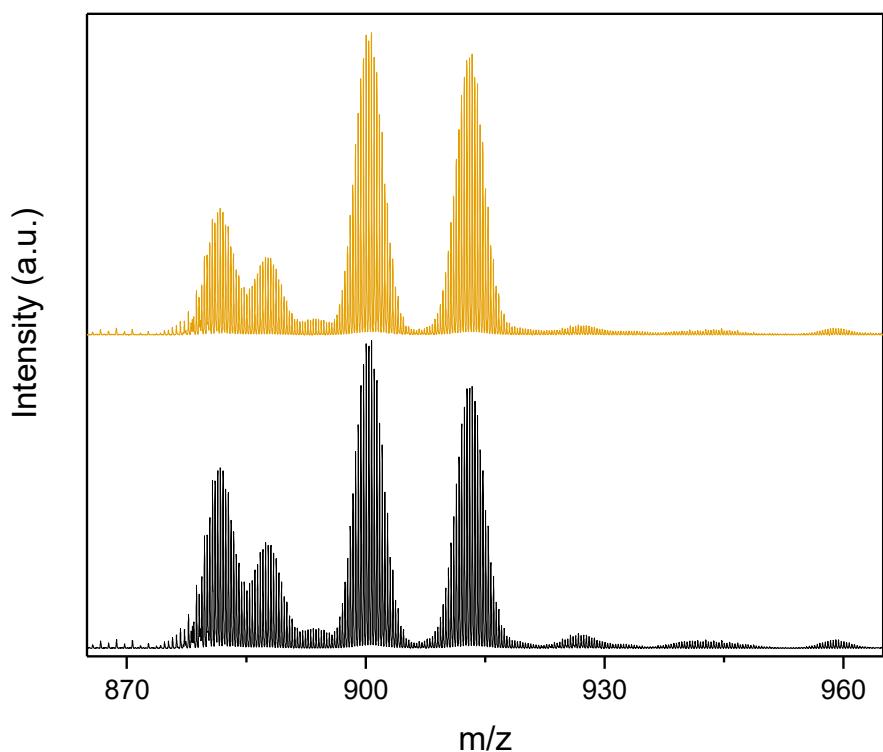
Figure S14. ESI-MS spectra for $PW_{11}O_{39}$ before (black) and after (orange) benzyl alcohol exposure. Reaction conditions for the adsorption experiments: V_{total} = 0.02 L deionized water with $C_{PW_{11}O_{39}}$ = 0.5 mM, $C_{alcohol}$ = 5 mM at room temperature for 10 min under magnetic stirring at 800 rpm.
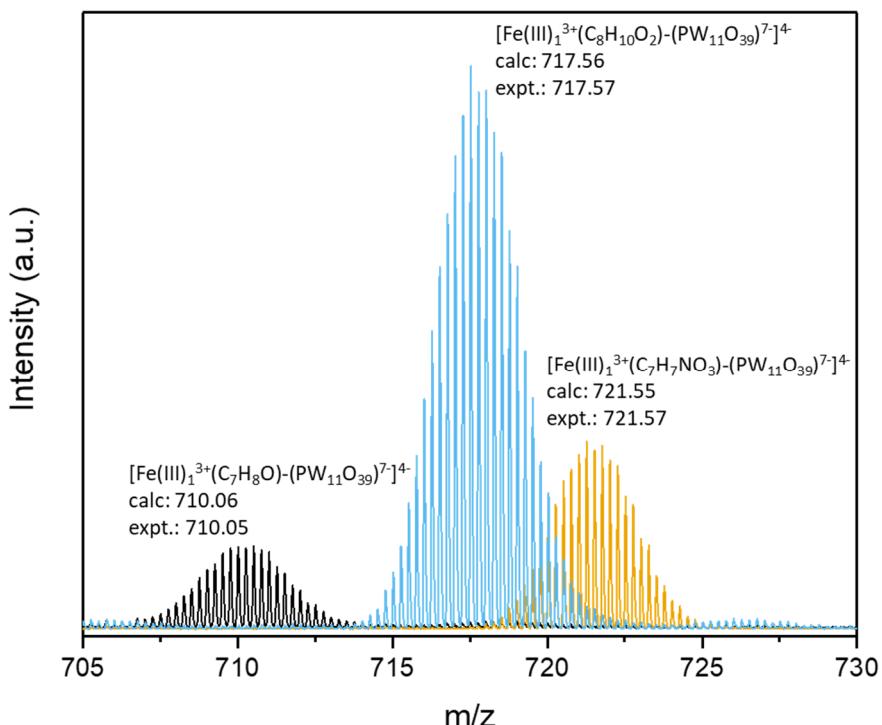
Figure S15. ESI-MS spectra of $PW_{11}O_{39}Fe_1$ mixed with different benzyl alcohol derivatives. The three used alcohols were: benzyl alcohol (black), 4-nitrobenzyl alcohol (orange), and 4-methoxybenzyl alcohol (light blue). Reaction conditions for the adsorption experiments: V_{total} = 0.02 L deionized water with $C_{PW_{11}O_{39}}$ = 0.5 mM, C_{Fe} = 0.5 mM, $C_{alcohol}$ = 5 mM at room temperature for 10 min under magnetic stirring at 800 rpm. Samples for the adsorption reaction solutions were immediately injected into the ESI-MS with delays < 30 s.
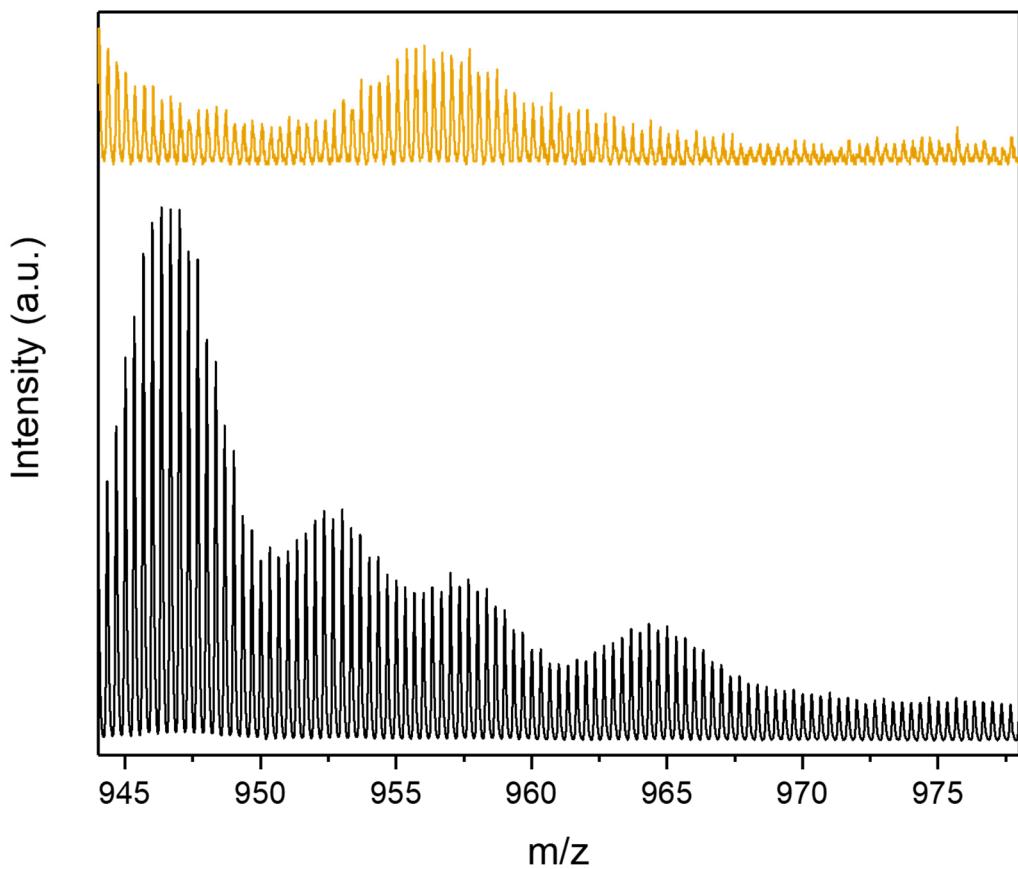
Figure S16. ESI-MS spectra for $PW_{11}O_{39}Fe_1$ before and during benzyl alcohol oxidation reaction. Spectra are shown for $PW_{11}O_{39}Fe_1$ during (black) and before (orange) benzyl oxidation reaction. Reaction conditions: V_{total} = 0.02 L deionized water with $C_{PW_{11}O_{39}}$ = 0.5 mM, C_{Fe} = 0.5 mM, C_{BnzOH} = 25 mM, and $C_{H_2O_2}$ = 50 mM at T = 70 °C under magnetic stirring at 800 rpm. For the reference experiment (orange), no benzyl alcohol and hydrogen peroxide were added into the reaction mixture, other conditions were the same. Samples from the reaction solutions were immediately injected into the ESI-MS with delays < 30 s. Prominent peaks at around m/z 957 and 964 could be observed for $PW_{11}O_{39}Fe_1$ which have been marked with asterisks in the main text.
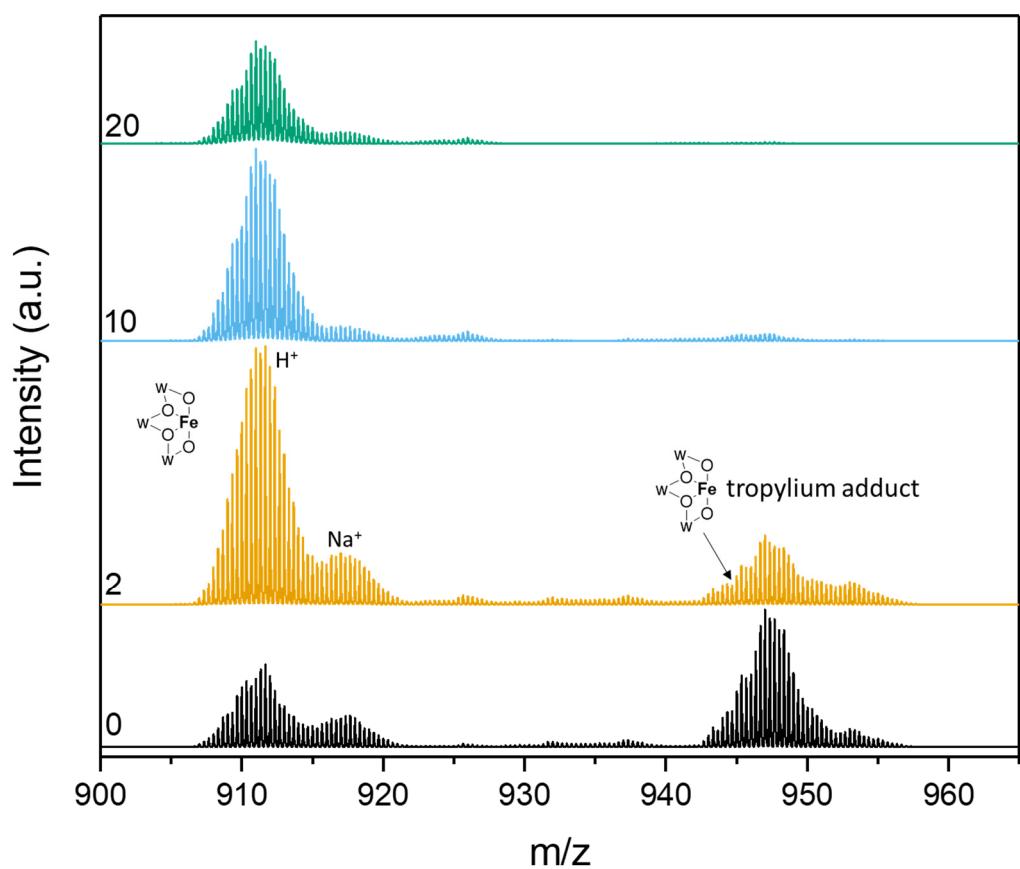
Figure S17. ESI-MS fragmentation pattern for $\{[Fe(III)_1{}^{3+}(C_7H_6O)\text{-}(PW_{11}O_{39})^{7-}] + H^+\}^{3-}$. The intermediate appeared to be relatively instable and strong fragmentation was visible at collision energies of 2 eV. This highlights the low stability of the aldehyde-bound intermediate against reaction product desorption.
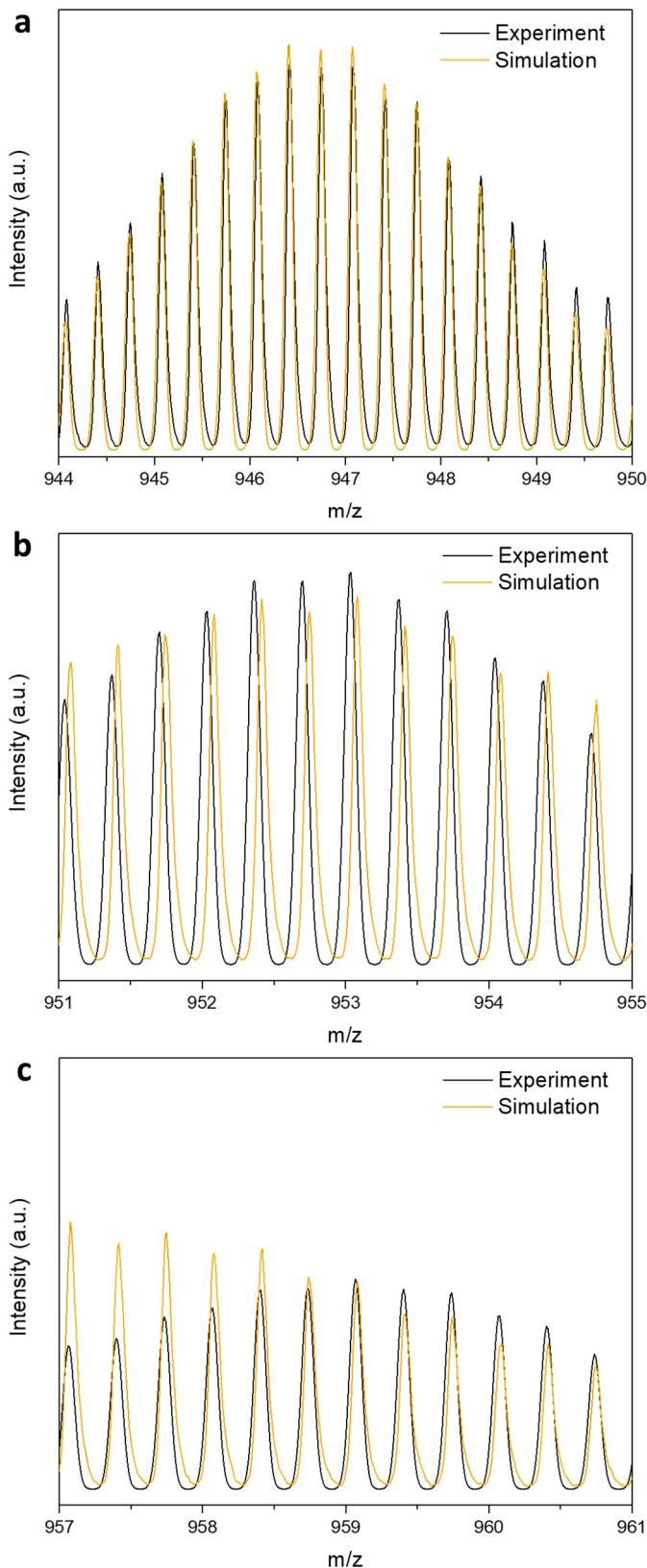
Figure S18. ESI-MS spectra and simulated pattern for different intermediates during the $PW_{11}O_{39}Fe_1$-catalysed benzyl alcohol oxidation reaction. (a) $\{[Fe(III)_1{}^{3+}(C_7H_6O)\text{-}(PW_{11}O_{39})^{7\text{-}}] + H^+\}^{3\text{-}}$ (**b-V**), (b) $\{[Fe(V)_1{}^{5+}(O^{2\text{-}})(C_7H_8O)\text{-}(PW_{11}O_{39})^{7\text{-}}] + H^+\}^{3\text{-}}$ (**b-III**), and (c) $\{[Fe(III)_1{}^{3+}(OOH^-)(C_7H_8O)\text{-}(PW_{11}O_{39})^{7\text{-}}] + 2H^+\}^{3\text{-}}$ (**b-II**). Slight mismatch can be observed for panel (b) but it is well within experimental errors.
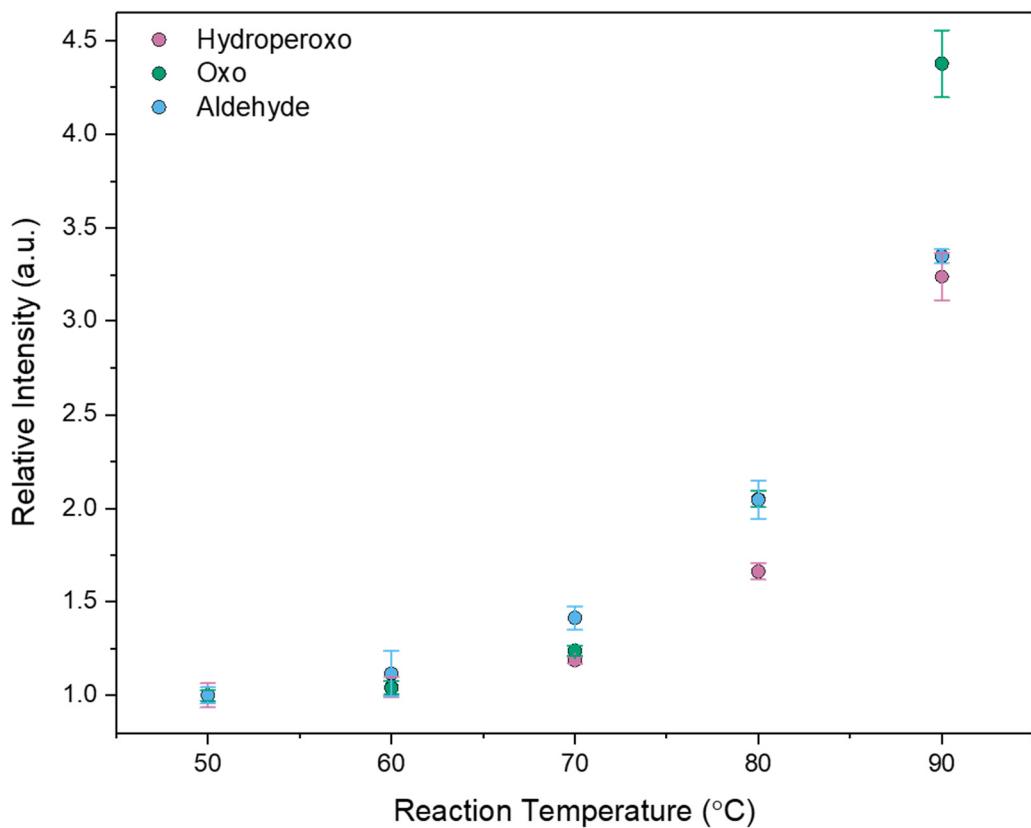
Figure S19. Kinetic ESI-MS for the $PW_{11}O_{39}Fe_1$-catalysed benzyl alcohol oxidation. ESI-MS intensities for the three most dominant peaks for each of the intermediates relative to the intensities at 50 °C. Exact formula for: Fe hydroperoxo intermediate $\{[Fe(III)_1^{3+}(OOH^-)(C_7H_8O)-(PW_{11}O_{39})^{7-}] + 2H^+\}^{3-}$, Fe oxo intermediate $\{[Fe(V)_1^{5+}(O^{2-})(C_7H_8O)-(PW_{11}O_{39})^{7-}] + H^+\}^{3-}$, and aldehyde-bound catalyst state $\{[Fe(III)_1^{3+}(C_7H_6O)-(PW_{11}O_{39})^{7-}] + H^+\}^{3-}$. Reaction conditions: V_{total} = 0.02 L deionized water with $C_{PW_{11}O_{39}}$ = 0.5 mM, C_{Fe} = 0.5 mM, C_{BnzOH} = 25 mM, and $C_{H_2O_2}$ = 50 mM at T = 60 °C – 90 °C under magnetic stirring at 800 rpm. Standard deviations are determined from measuring the relative intensities for 3 different peaks belonging to the same species.

{[Fe(III)$_1$$^{3+}$(C$_7H_5NO_3$)-(PW$_{11}O_{39}$)$^{7-}$] + H$^+$}$^{3-}$
calc.: 961.74
expt.: 961.74

{[Fe(III)$_1$$^{3+}$(OOH$^-$)(C$_7H_7NO_3$)-(PW$_{11}O_{39}$)$^{7-}$] + 2H$^+$}$^{3-}$
calc.: 974.74
expt.: 974.74

{[Fe(V)$_1$$^{5+}$(O^{2-})(C$_7H_7NO_3$)-(PW$_{11}O_{39}$)$^{7-}$] + H$^+$}$^{3-}$
calc.: 968.07
expt.: 968.06

{[Fe(III)$_1$$^{3+}$(OOH$^-$)(C$_7H_7NO_3$)-(PW$_{11}O_{39}$)$^{7-}$] + Na$^+$ + K$^+$}$^{3-}$
calc.: 994.06
expt.: 994.04

{[Fe(III)$_1$$^{3+}$(OOH$^-$)(C$_7H_7NO_3$)-(PW$_{11}O_{39}$)$^{7-}$] + 2Na$^+$}$^{3-}$
calc.: 988.06
expt.: 988.04
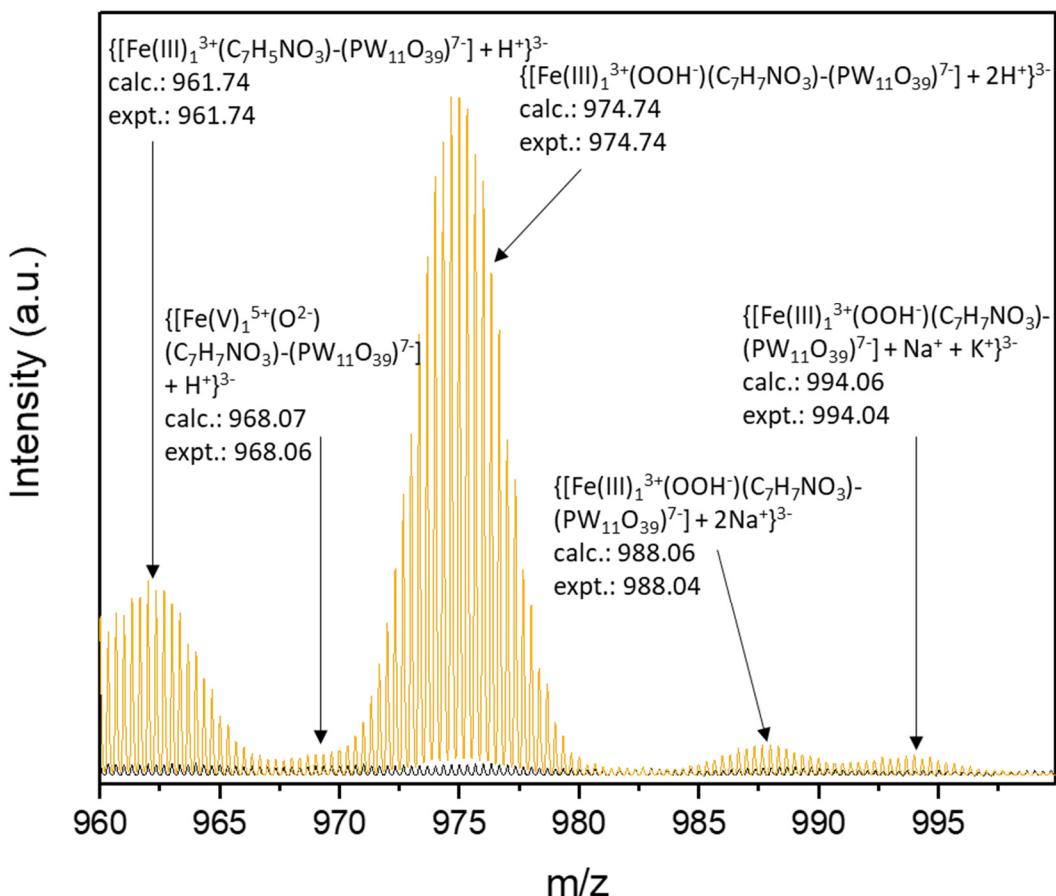
**Figure S20.** ESI-MS spectra for the PW$_{11}$O$_{39}$Fe$_1$-catalysed 4-nitrobenyzl alcohol oxidation. Overlap of PW$_{11}$O$_{39}$Fe$_1$ before (black) and after reaction (orange) with 4-nitrobenzyl alcohol. Reaction conditions: V_{total} = 0.02 L deionized water with $C_{PW_{11}O_{39}}$ = 0.5 mM, C_{Fe} = 0.5 mM, $C_{4-nitroBnzOH}$ = 25 mM, and $C_{H_2O_2}$ = 50 mM at T = 30 °C under magnetic stirring at 800 rpm.

{[Fe(III)$_1^{3+}$(C$_8$H$_8$O$_2$)-(PW$_{11}$O$_{39}$)$^{7-}$] + H$^+$}$^{3-}$
calc: 957.08
expt.: 957.08

{[Fe(V)$_1^{5+}$(O^{2-})(C$_8$H$_{10}$O$_2$)-(PW$_{11}$O$_{39}$)$^{7-}$] + H$^+$}$^{3-}$
calc: 962.74
expt.: 962.75

{[Fe(III)$_1^{3+}$(OOH$^-$)(C$_8$H$_{10}$O$_2$)-(PW$_{11}$O$_{39}$)$^{7-}$] + 2H$^+$}$^{3-}$
calc: 968.08
expt.: 968.08
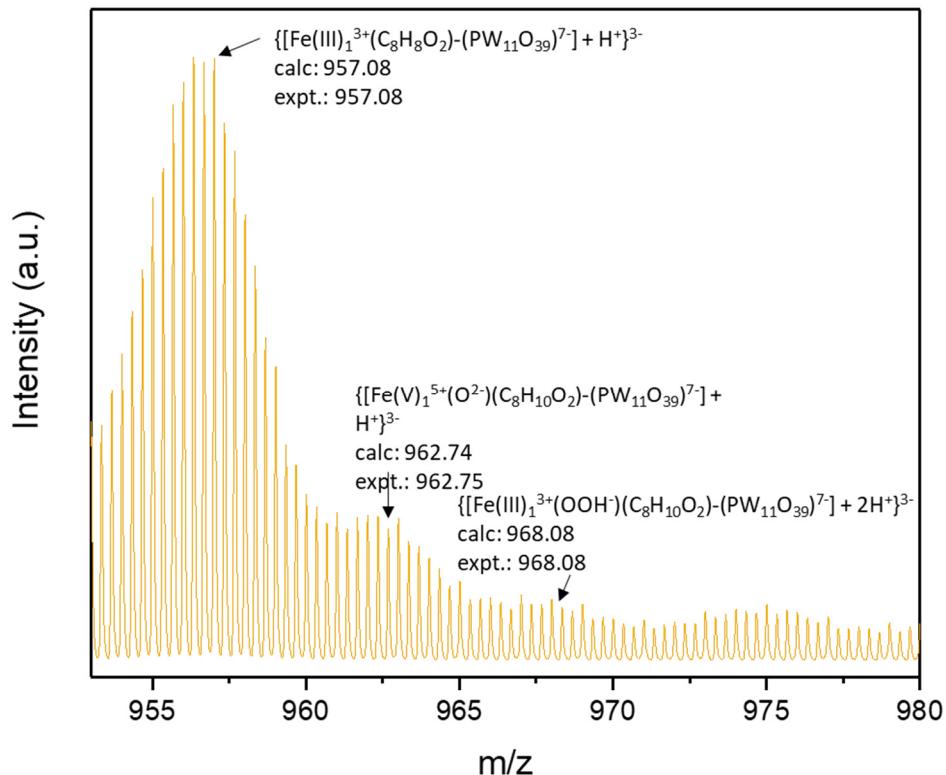
Figure S21. ESI-MS spectra for the 4-methoxybenzyl alcohol oxidation reaction with PW$_{11}$O$_{39}$Fe$_1$. Reaction conditions: V_{total} = 0.02 L deionized water with $C_{PW_{11}O_{39}}$ = 0.5 mM, C_{Fe} = 0.5 mM, $C_{4-methoxyBnzOH}$ = 25 mM, and $C_{H_2O_2}$ = 50 mM at T = 70 °C for 0.5 h under magnetic stirring at 800 rpm. The same key intermediates compared with the benzyl alcohol oxidation reaction were observed. Relative intensities, however, are slightly different due to dissimilar reactivities of both substrates.
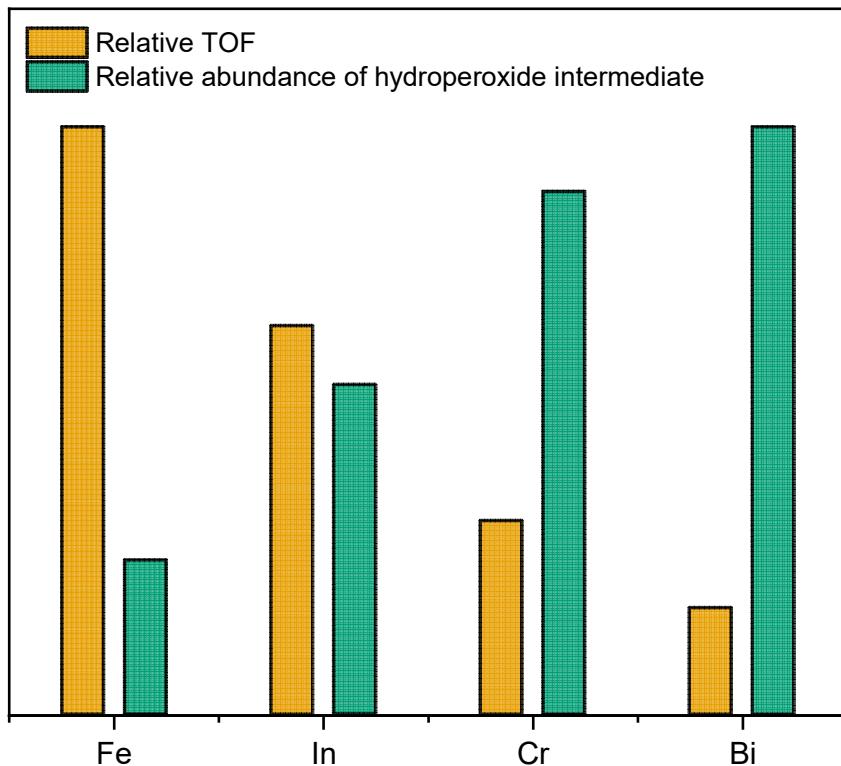
Figure S22. Correlation between the relative abundance of the hydroperoxo intermediate and the turnover frequency for the benzyl alcohol oxidation reaction. V_{total} = 0.02 L deionized water with $C_{PW_{11}O_{39}}$ = 0.5 mM, C_{Fe} = 0.5 mM, $C_{4-nitroBnzOH}$ = 25 mM, and $C_{H_2O_2}$ = 50 mM at T = 30 °C under magnetic stirring at 800 rpm. The abundance of the hydroperoxo intermediate is shown relative to the $PW_{11}O_{39}M_1$ peak; observed hydroperoxo intermediates ($\{M(III)_1^{3+}(OOH^-)(C_7H_8O)\text{-}(PW_{11}O_{39})^{7-} + 2H^+\}^{3-}$ (M = Fe, calc.: 958.07, expt.: 958.00; M = In, calc.: 978.40, expt.: 957.39; M = Cr, calc.: 957.42, expt.: 957.39; M = Bi, calc.: 1009.75, expt.: 1009.76) for all four catalysts. TOF values are extracted from Table S3.

For a more quantitative correlation between ESI-MS and the catalytic activity of $PW_{11}O_{39}M_1$ in the benzyl alcohol oxidation reaction, we used a methodology developed by Reek et al.[2b] They proposed that the catalytic activity can be predicted based on the abundance of the intermediate right before the rate-determining step. In principle, a lower abundance of the species before the rate-determining step would hint at a lower activation barrier and thus higher reactivity. For catalysts following the same reaction mechanism and thus exhibiting the same intermediates, the abundance of the common hydroperoxo species was measured during the benzyl alcohol oxidation reaction. Indeed, a good inverse correlation between the abundance of the hydroperoxo species and the turnover frequency was observed (Fig. S 22) further confirming that ESI-MS is a tool to not only determine reaction mechanisms qualitatively but also able to describe catalytic activity of different catalysts in a (semi-)quantitative way.
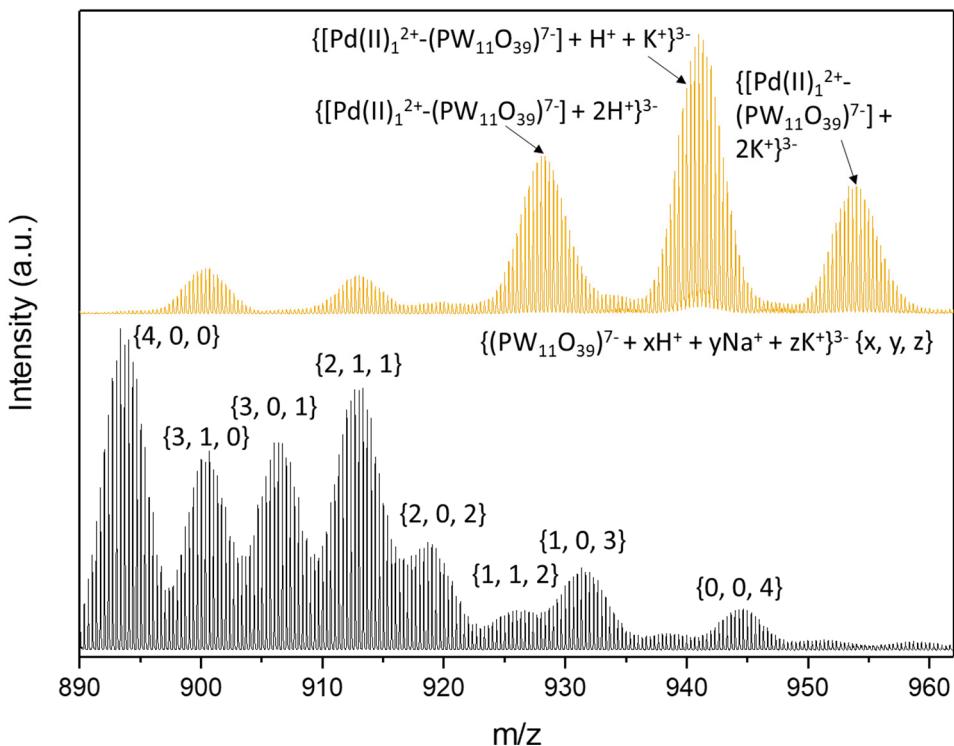
Figure S23. ESI-MS spectra for $PW_{11}O_{39}$ and $PW_{11}O_{39}Pd_1$. $PW_{11}O_{39}$ (black) with the respective cation envelope for z = 3. $PW_{11}O_{39}Pd_1$ (orange) with a much-reduced cation envelope due to the adsorption of divalent Pd(II). Surprisingly, the formation of Na adducts did not occur to a significant extent.

SACs based on elements that are located on the right of the so-called oxo-wall[15]—the border between metals forming oxo species and those that do not—are expected to follow a distinct mechanism in the benzyl alcohol oxidation reaction compared with Fe-based SAC. To explore whether ESI-MS is able to differentiate the two, we probed the reaction mechanism of $PW_{11}O_{39}Pd_1$ (Figure S23), which was the most active SAC containing noble metals (TOF = 5 h^{-1} at 70 °C, Table S2). During the benzyl alcohol oxidation, distinct intermediates were observed (Figure S24) including the water-containing complex $\{[Pd(II)_1{}^{2+}(C_7H_8O)(H_2O)\text{-}(PW_{11}O_{39})^{7-}] + 3H^+\}^{2-}$ (c-II, calc.: 1456.61, expt.: 1456.56). This complex likely formed from the compound c-I which was not observed in the case of benzyl alcohol but only when 4-nitrobenzyl alcohol was used. $PW_{11}O_{39}Pd_1$ then underwent heterolytic cleavage of H_2O_2 to form $\{[Pd(II)_1{}^{2+}(C_7H_8O)(H_2O)\text{-}(PW_{11}O_{39})^{7-}(OH^-)] + 3H^+ + Na^+\}^{2-}$ (c-III, calc.: 1476.61, expt.: 1476.56) probably involving tungsten hydroperoxides that have been described before on POM-based catalysts.[16] The dehydrogenation step of benzyl alcohol then involved a hydride transfer to Pd while the tungsten hydroperoxide was cleaved forming $\{[Pd(II)_1{}^{2+}(H^-)(C_7H_6O)(H_2O)\text{-}(PW_{11}O_{39})^{7-}] + H^+ + Na^+ + 2K^+\}^{2-}$ (c-IV, calc.: 1506.06, expt.: 1506.01). Species c-II was presumably reformed by one of those two pathways, either the insertion of O_2 (c-VI) and decomposition of the hydroperoxo species,[17] or the deprotonation to c-VII and subsequent elimination of water[18] c-VIII which would require reoxidation of Pd^0 before the catalytic cycle was closed. The proposed catalytic cycle with all observed intermediates is shown in Figure S25. Reaction with 4-nitrobenzyl alcohol revealed a similar picture with details provided in the Supplementary information (Figure S26). The formation of $PW_{11}O_{39}Pd_1$ dimers in the solid state[19] has been reported before and based on ESI-MS

results, they appear to co-exist with monomeric species in our catalytic system as well. The formation of dimers seems to be concentration-dependent (Figure S27), and the dimer concentration during the benzyl alcohol oxidation reaction can be assumed to be relatively low. Further, DFT calculations suggest that the spontaneous decomposition of $PW_{11}O_{39}Pd_1$ dimers in the presence of weakly coordinating species like water is exothermic by -1.432 eV (Figure S28). Despite this, we cannot completely rule out the contribution of dimeric catalyst species to the overall catalytic activity.


$\{[Pd(II)_1{}^{2+}(C_7H_8O)(H_2O)-(PW_{11}O_{39})^{7-}] + 3H^+\}^{2-}$
calc.: 1456.61
expt.:1456.56

$\{[Pd(II)_1{}^{2+}(H^-)(C_7H_6O)(H_2O)-(PW_{11}O_{39})^{7-}] + H^+ + Na^+ + 2K^+\}^{2-}$
calc.: 1506.06
expt.:1506.01

$\{[Pd(II)_1{}^{2+}(C_7H_8O)(H_2O)-(PW_{11}O_{39})^{7-}(OH^-)] + 3H^+ + Na^+\}^{2-}$
calc.: 1476.61
expt.:1476.57
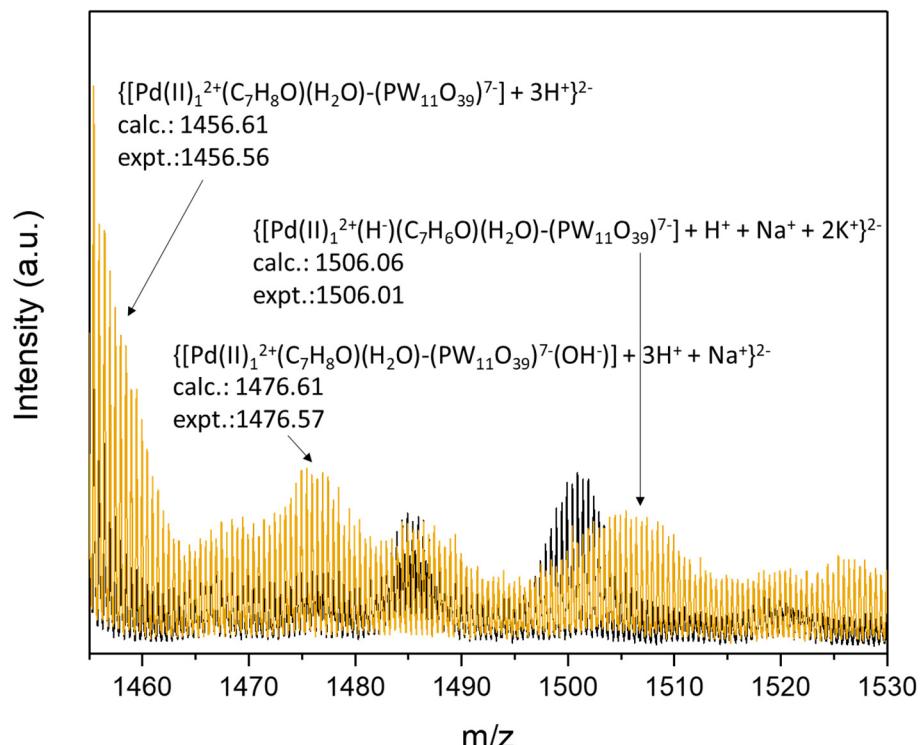
Figure S24. ESI-MS spectra for $PW_{11}O_{39}Pd_1$ before and after benzyl alcohol oxidation reaction. Spectra are shown for $PW_{11}O_{39}Pd_1$ before (black) and after (orange) benzyl oxidation reaction. Reaction conditions: V_{total} = 0.02 L deionized water with $C_{PW_{11}O_{39}}$ = 0.5 mM, C_{Pd} = 0.5 mM, C_{BnzOH} = 25 mM, and $C_{H_2O_2}$ = 50 mM at T = 70 °C for 5 h under magnetic stirring at 800 rpm.
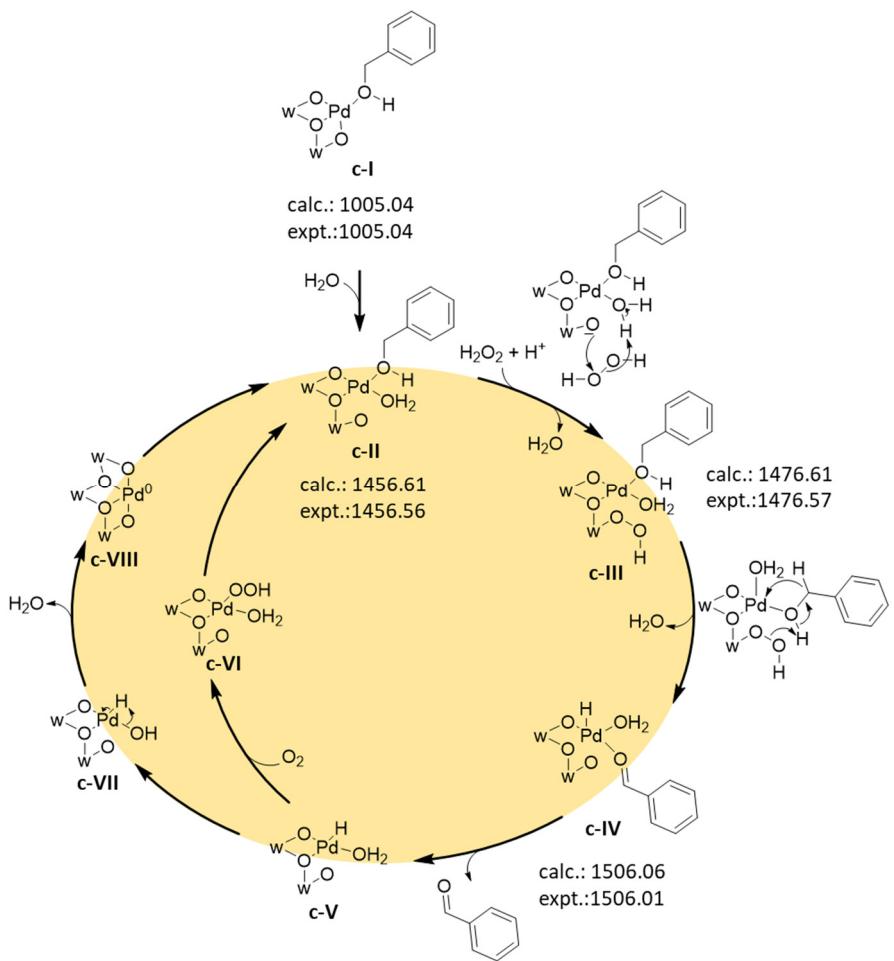
Figure S25. Proposed mechanism for the benzyl alcohol oxidation by $PW_{11}O_{39}Pd_1$. The catalytic cycle as determined by ESI-MS is shown here with the experimentally determined and simulated masses of different intermediates. Reoxidation of the Pd hydride species **c-V** was not observed by ESI-MS but can be expected to follow one of the two proposed reaction pathways.
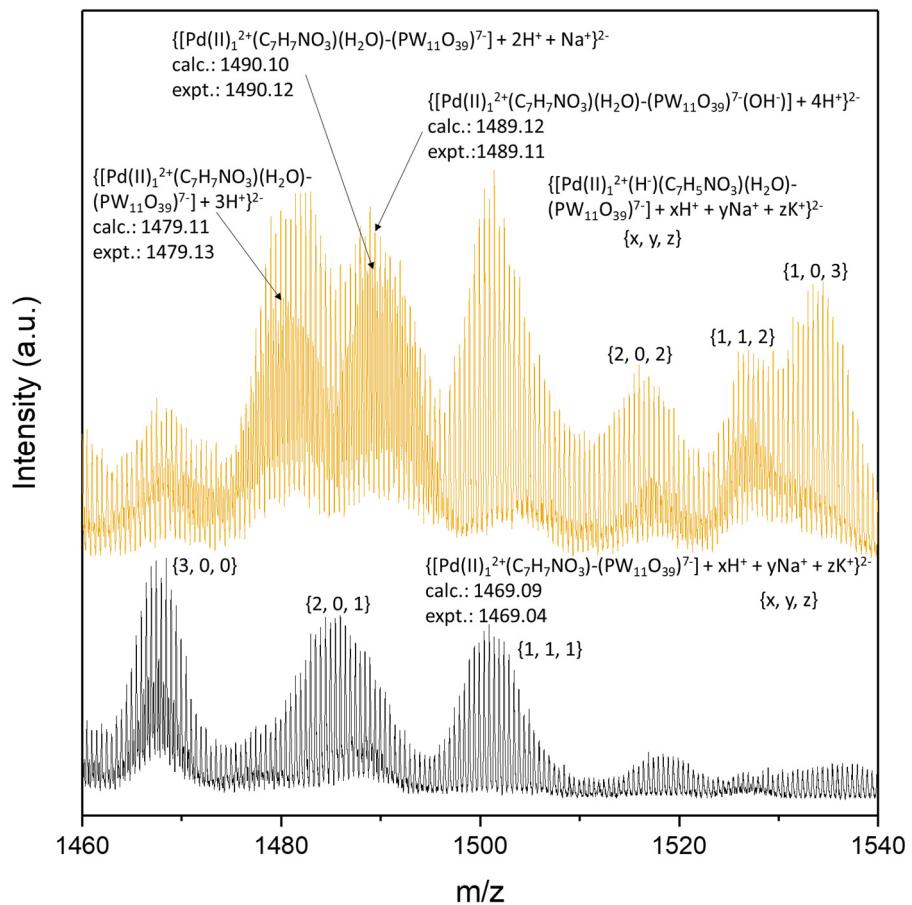
Figure S26. ESI-MS spectra for $PW_{11}O_{39}Pd_1$ before and after 4-nitrobenzyl alcohol oxidation reaction. Spectra are shown for $PW_{11}O_{39}Pd_1$ before (black) and after (orange) benzyl oxidation reaction. Reaction conditions: V_{total} = 0.02 L deionized water with $C_{PW_{11}O_{39}}$ = 0.5 mM, C_{Pd} = 0.5 mM, $C_{4-nitroBnzOH}$ = 25 mM, and $C_{H_2O_2}$ = 50 mM at T = 70 °C for 5 h under magnetic stirring at 800 rpm. The same intermediates as for the benzyl alcohol oxidation can be observed here albeit in higher concentrations. Due to the lower charge of Pd(II) compared to Fe(III), more individual peaks appeared making the analysis of the spectra more complicated.
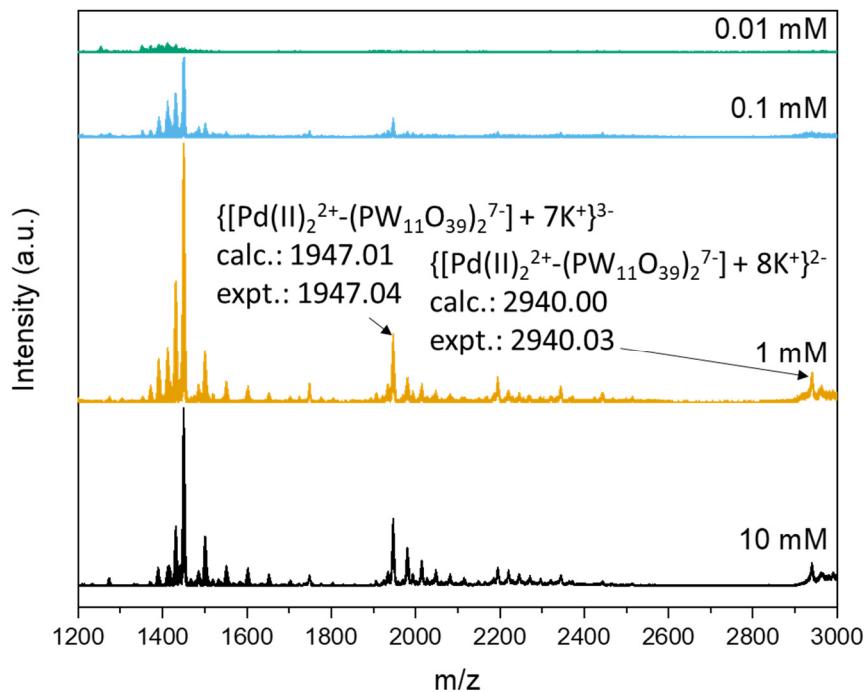
Figure S27. ESI-MS of a 1:1 molar ratio of $K_7PW_{11}O_{39}$ and $Pd(NO_3)_2$ showing the concentration dependent coexistence of $PW_{11}O_{39}Pd_1$ and $(PW_{11}O_{39})_2Pd_2$ species.
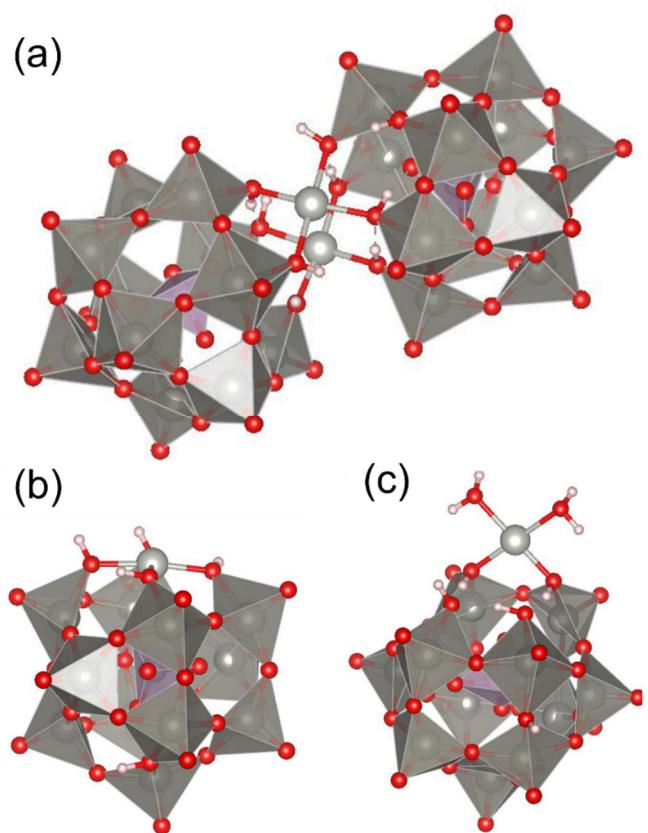
Figure S28. Optimized structure of $PW_{11}O_{39}Pd_1$ (a) dimers, (b) monomers, and (c) Pd with attached water molecules. The molecules are all charge balanced by protons to reflect the structure in solution. We have sampled the positions of the protons, partially for the neighboring sites of the Pd. 102, 44, and 59 different structures have been optimized for (a), (b) and (c) respectively for locating the putative optimal locations of protons.

Supplementary References

[1] R. Contant, *Can. J. Chem.* **1987**, *65*, 568-573.

[2] a) C. Markert, A. Pfaltz, *Angew. Chem. Int. Ed.* **2004**, *43*, 2498-2500; b) J. Wassenaar, E. Jansen, W.-J. van Zeist, F. M. Bickelhaupt, M. A. Siegler, A. L. Spek, J. N. H. Reek, *Nat. Chem.* **2010**, *2*, 417-421.

[3] a) J. Hutter, M. Iannuzzi, F. Schiffmann, J. VandeVondele, *WIREs Comput. Mol. Sci.* **2014**, *4*, 15-25; b) J. VandeVondele, J. Hutter, *J. Chem. Phys.* **2007**, *127*, 114105.

[4] a) G. Kresse, J. Furthmüller, *Comput. Mat. Sci.* **1996**, *6*, 15-50; b) G. Kresse, J. Furthmüller, *Phys. Rev. B* **1996**, *54*, 11169-11186; c) G. Kresse, J. Hafner, *Phys. Rev. B* **1993**, *47*, 558-561; d) G. Kresse, J. Hafner, *Phys. Rev. B* **1994**, *49*, 14251-14269.

[5] A. Hjorth Larsen, J. Jørgen Mortensen, J. Blomqvist, I. E. Castelli, R. Christensen, M. Dułak, J. Friis, M. N. Groves, B. Hammer, C. Hargus, E. D. Hermes, P. C. Jennings, P. Bjerre Jensen, J. Kermode, J. R. Kitchin, E. Leonhard Kolsbjerg, J. Kubal, K. Kaasbjerg, S. Lysgaard, J. Bergmann Maronsson, T. Maxson, T. Olsen, L. Pastewka, A. Peterson, C. Rostgaard, J. Schiøtz, O. Schütt, M. Strange, K. S. Thygesen, T. Vegge, L. Vilhelmsen, M. Walter, Z. Zeng, K. W. Jacobsen, *J. Phys. Condens. Matter* **2017**, *29*, 273002.

[6] a) G. Henkelman, H. Jónsson, *J. Chem. Phys.* **2000**, *113*, 9978-9985; b) G. Henkelman, B. P. Uberuaga, H. Jónsson, *J. Chem. Phys.* **2000**, *113*, 9901-9904; c) S. Smidstrup, A. Pedersen, K. Stokbro, H. Jónsson, *J. Chem. Phys.* **2014**, *140*, 214106.

[7] G. Henkelman, H. Jónsson, *J. Chem. Phys.* **1999**, *111*, 7010-7022.

[8] J. P. Perdew, K. Burke, M. Ernzerhof, *Phys. Rev. Lett.* **1996**, *77*, 3865-3868.

[9] J. M. Maestre, X. Lopez, C. Bo, J.-M. Poblet, N. Casañ-Pastor, *J. Am. Chem. Soc.* **2001**, *123*, 3749-3758.

[10] X. López, J. J. Carbó, C. Bo, J. M. Poblet, *Chem. Soc. Rev.* **2012**, *41*, 7537-7571.

[11] N. E. Schultz, Y. Zhao, D. G. Truhlar, *J. Phys. Chem. A* **2005**, *109*, 11127-11143.

[12] H.-N. Wu, J. Wang, H. Li, N.-N. Ma, T. Zhang, S.-Q. Shi, L.-K. Yan, Z.-M. Su, *Comput. Theor. Chem.* **2016**, *1089*, 28-34.

[13] X. Wu, T. Huang, Q. Wu, L. Xu, *Dalton Trans.* **2016**, *45*, 271-275.

[14] a) T. A. Manz, N. G. Limas, *RSC Adv.* **2016**, *6*, 47771-47801; b) N. G. Limas, T. A. Manz, *RSC Adv.* **2016**, *6*, 45727-45747; c) T. A. Manz, *RSC Adv.* **2017**, 7, 45552-45581; d) N. G. Limas, T. A. Manz, *RSC Adv.* **2018**, *8*, 2678-2707; e) T. A. Manz, D. S. Sholl, *J. Chem. Theory Comput.* **2012**, *8*, 2844-2867.

[15] E. Andris, R. Navrátil, J. Jašík, M. Puri, M. Costas, L. Que, J. Roithová, *J. Am. Chem. Soc.* **2018**, *140*, 14391-14400.

[16] C. Ci, H. Liu, L. Yan, Z. Su, *ChemistryOpen* **2016**, *5*, 470-476.

[17] M. C. Denney, N. A. Smythe, K. L. Cetto, R. A. Kemp, K. I. Goldberg, *J. Am. Chem. Soc.* **2006**, *128*, 2508-2509.

[18] D. Milstein, J. C. Calabrese, I. D. Williams, *J. Am. Chem. Soc.* **1986**, *108*, 6387-6389.

[19] N. V. Izarova, A. Banerjee, U. Kortz, *Inorg. Chem.* **2011**, *50*, 10379-10386.